



BINARY CLASSIFICATION OF AN UNKNOWN OBJECT  
THROUGH ATMOSPHERIC TURBULENCE USING A POLARIMETRIC  
BLIND-DECONVOLUTION ALGORITHM AUGMENTED  
WITH ADAPTIVE DEGREE OF LINEAR POLARIZATION PRIORS

THESIS

Mu J. Kim, Captain, USAF,

AFIT/GE/ENG/12-26

DEPARTMENT OF THE AIR FORCE  
AIR UNIVERSITY

**AIR FORCE INSTITUTE OF TECHNOLOGY**

Wright-Patterson Air Force Base, Ohio

APPROVED FOR PUBLIC RELEASE; DISTRIBUTION UNLIMITED.

The views expressed in this thesis are those of the author and do not reflect the official policy or position of the United States Air Force, Department of Defense, or the United States Government. This material is declared a work of the U.S. Government and is not subject to copyright protection in the United States.

BINARY CLASSIFICATION OF AN UNKNOWN OBJECT  
THROUGH ATMOSPHERIC TURBULENCE USING A POLARIMETRIC  
BLIND-DECONVOLUTION ALGORITHM AUGMENTED  
WITH ADAPTIVE DEGREE OF LINEAR POLARIZATION PRIORS

THESIS

Presented to the Faculty  
Department of Electrical and Computer Engineering  
Graduate School of Engineering and Management  
Air Force Institute of Technology  
Air University  
Air Education and Training Command  
In Partial Fulfillment of the Requirements for the  
Degree of Master of Science in Electrical Engineering

Mu J. Kim, Captain, USAF, B.S.E.E.

March 2012

APPROVED FOR PUBLIC RELEASE; DISTRIBUTION UNLIMITED.

BINARY CLASSIFICATION OF AN UNKNOWN OBJECT  
THROUGH ATMOSPHERIC TURBULENCE USING A POLARIMETRIC  
BLIND-DECONVOLUTION ALGORITHM AUGMENTED  
WITH ADAPTIVE DEGREE OF LINEAR POLARIZATION PRIORS

Mu J. Kim, Captain, USAF, B.S.E.E.

Approved:

/signed/

1 Mar 2012

\_\_\_\_\_  
Maj. Milo W. Hyde IV, PhD (Chairman)

\_\_\_\_\_  
date

/signed/

1 Mar 2012

\_\_\_\_\_  
Dr. Stephen C. Cain (Member)

\_\_\_\_\_  
date

/signed/

1 Mar 2012

\_\_\_\_\_  
Dr. Michael A. Marciniak (Member)

\_\_\_\_\_  
date

*Abstract*

In this research, an improved binary material-classification algorithm is developed to discriminate between metals and dielectrics using passive polarimetric imagery degraded by atmospheric turbulence. The technique implements a modified version of an existing polarimetric blind-deconvolution algorithm in order to remove atmospheric distortion and correctly classify the unknown object. The classification decision is based on degree of linear polarization (DoLP) estimates provided by the blind-deconvolution algorithm augmented with two DoLP priors—one statistically modeling the polarization behavior of metals and the other statistically modeling the polarization behavior of dielectrics. The proposed algorithm significantly improves upon a similar published polarimetric classification method by adaptively updating the DoLP priors as more information becomes available about the scene.

Three approaches for implementing the adaptive DoLP priors are presented—the higher-order super-Gaussian method, the Gaussian method, and the distribution-averaging method. The higher-order super-Gaussian method fits the distribution of the in-progress DoLP estimates from the blind-deconvolution algorithm with a sum of two super-Gaussian functions. The results of the nonlinear fit are then used to form the DoLP priors. The Gaussian method fits the distribution of DoLP estimates with the sum of two Gaussian functions to compute a classification threshold value. The resulting threshold is then used to update the DoLP priors. The distribution-averaging method approximates the threshold value by finding the mean of the DoLP distribution. Using this threshold value, the DoLP priors are then formed. The proposed technique is experimentally validated by comparing classification results of a dielectric and metallic sample obtained using the new method to those obtained using the existing approach. The experimental results confirm that the new adaptive method significantly extends the range of validity of the existing polarimetric

classification technique to near-normal collection geometries where most polarimetric material classifiers perform poorly.

## *Acknowledgements*

First and foremost I would like to thank my thesis advisor, Maj. Milo Hyde, for his sound teaching, encouragement, and inspiration. His guidance and support enabled me to understand the subject, and his detailed and constructive comments helped me in writing the thesis. This thesis would not have been possible without his advice. I am also grateful to the rest of my thesis committee, Dr. Stephen Cain and Dr. Michael Marciniak, for reviewing this document and providing insightful comments. I am indebted to my colleagues in the OPTECS laboratory for their kind support as well. Lastly, and most importantly, I wish to thank my wife for her love and support.

Mu J. Kim, Captain, USAF

## *Table of Contents*

	Page
Abstract . . . . .	iv
Acknowledgements . . . . .	vi
Table of Contents . . . . .	vii
List of Figures . . . . .	ix
List of Tables . . . . .	xi
List of Abbreviations . . . . .	xii
 I. Introduction . . . . .	 1
1.1 Goals . . . . .	2
1.2 Assumptions . . . . .	3
1.3 Thesis Outline . . . . .	4
 II. Background . . . . .	 5
2.1 Polarization . . . . .	5
2.1.1 Polarization State . . . . .	5
2.1.2 Stokes Vectors and Mueller Matrices . . . . .	7
2.2 Imaging . . . . .	9
2.2.1 Incoherent Imaging . . . . .	9
2.2.2 The OTF of a Diffraction-Limited Incoherent Imaging System . . . . .	10
2.2.3 Atmospheric Turbulence . . . . .	11
2.2.4 Imaging through Turbulence . . . . .	11
2.3 Blind Deconvolution . . . . .	14
2.3.1 Maximum-Likelihood Estimation . . . . .	15
2.3.2 Expectation-Maximization Algorithm . . . . .	15
2.4 Multiframe Blind-Deconvolution . . . . .	16
2.5 Multichannel Blind Deconvolution of Polarimetric Imagery . . . . .	19
2.6 Classifying the Material of an Unknown Object with DoLP Priors . . . . .	24
2.6.1 DOLP Priors . . . . .	24
2.6.2 Limitations . . . . .	28



	Page
III. Research Methodology . . . . .	30
3.1 Material Classification . . . . .	30
3.2 Adaptive DoLP Priors . . . . .	31
3.2.1 Higher-Order Super-Gaussian Method . . . . .	32
3.2.2 Gaussian method . . . . .	33
3.2.3 Distribution-Averaging Method . . . . .	35
3.3 Algorithm Execution . . . . .	36
IV. Results and Analysis . . . . .	39
4.1 Experimental Setup . . . . .	39
4.2 Classification Results—Fixed DoLP Priors . . . . .	40
4.3 Classification Results—Adaptive DoLP Priors . . . . .	43
4.3.1 Higher-Order Super-Gaussian Method . . . . .	43
4.3.2 Gaussian Method . . . . .	43
4.3.3 Distribution-Averaging Method . . . . .	46
4.4 Spatial Analysis of the Classification Results . . . . .	47
V. Conclusions and Future Work . . . . .	50
5.1 Conclusions . . . . .	50
5.2 Future Work . . . . .	51
5.2.1 Testing Collection Geometry Region of Validity . . . . .	51
5.2.2 Field Testing . . . . .	51
5.2.3 Comparison of Material-Classification Results . . . . .	51
5.2.4 Use of $S_0$ Estimate to Aid Classification . . . . .	52
5.2.5 DoLP Derivative Classification . . . . .	52
5.2.6 Diffraction-Limited Truth Images . . . . .	53
Bibliography . . . . .	54

## *List of Figures*

Figure		Page
2.1.	Illustration of the polarization ellipse rotated through angle $\psi$ .	6
2.2.	Effect of atmospheric turbulence on imaging. . . . .	14
2.3.	ML estimation results using Schulz's parameterized-PSF blind-deconvolution algorithm. . . . .	20
2.4.	ML estimation results using three-channel ( $0^\circ, 60^\circ, 120^\circ$ ) polarimetric imagery. . . . .	23
2.5.	DoLP priors modeled with a super-Gaussian distribution. . . .	25
2.6.	Estimation results using four-channel ( $0^\circ, 45^\circ, 90^\circ, 135^\circ$ ) polarimetric imagery. . . . .	28
2.7.	Binary material classification of an unknown object. . . . .	29
3.1.	(a) Distribution of measured DoLP at $\theta_i = 50^\circ$ . (b) Distribution of measured DoLP at $\theta_i = 24^\circ$ . . . . .	32
3.2.	Higher-order super-Gaussian method for adaptive DoLP priors	33
3.3.	PDF of the division of two Poisson random variables using Monte Carlo analysis. . . . .	34
3.4.	Gaussian method for adaptive DoLP priors . . . . .	35
3.5.	Distribution-averaging method for adaptive DoLP priors . . . .	36
3.6.	Flowchart of the proposed material-classification algorithm augmented with adaptive DoLP priors at the $i^{\text{th}}$ iteration. . . . .	37
3.7.	(a) RMSE of DoLP to determine the iteration number to update DoLP priors. (b) RMSE of $S_0$ to determine the stopping criterion for the material-classification algorithm. . . . .	38
4.1.	Photograph of the Stokes polarimeter used to collect the polarimetric imagery in this experiment [11]. . . . .	39
4.2.	Results of Hyde's material-classification algorithm for the painted aluminum target ( $D/r_0 \approx 7.9$ and $\theta_i = \theta_r = 50^\circ$ ). . . . .	41
4.3.	Results of Hyde's material-classification algorithm for the painted aluminum target ( $D/r_0 \approx 7.9$ and $\theta_i = \theta_r = 24^\circ$ ). . . . .	42

Figure		Page
4.4.	Results of the material-classification algorithm using adaptive DoLP priors derived from the higher-order super-Gaussian method for the painted aluminum target ( $\theta_i = \theta_r = 24^\circ$ and $D/r_0 \approx 7.9$ ).	44
4.5.	Results of the material-classification algorithm using adaptive DoLP priors derived from the Gaussian method for the painted aluminum target ( $\theta_i = \theta_r = 24^\circ$ and $D/r_0 \approx 7.9$ ). . . . .	45
4.6.	Results of the material-classification algorithm using adaptive DoLP priors derived from the distribution-averaging method for the painted aluminum target ( $\theta_i = \theta_r = 24^\circ$ and $D/r_0 \approx 7.9$ ). .	46
5.1.	A three-channel polarization camera developed by FluxData, Inc.	52

# *List of Tables*

Table		Page
4.1.	Material-classification results for the painted aluminum target at $\theta_i = \theta_r = 24^\circ$ . . . . .	48

## *List of Abbreviations*

Abbreviation		Page
RADAR	Radio Detection and Ranging . . . . .	1
LADAR	Laser Detection and Ranging . . . . .	1
DoLP	Degree of Linear Polarization . . . . .	2
AoP	Angle of Polarization . . . . .	3
PSF	Point Spread Function . . . . .	9
OTF	Optical Transfer Function . . . . .	10
MTF	Modulation Transfer Function . . . . .	10
OPL	Optical Path Length . . . . .	11
ML	Maximum Likelihood . . . . .	14
PDF	Probability Density Function . . . . .	15
EM	Expectation Maximization . . . . .	15
SNR	Signal-to-Noise Ratio . . . . .	19
MAP	Maximum <i>A Posteriori</i> . . . . .	24
pBRDF	Polarimetric Bidirectional Reflectance Distribution Function	24
RMSE	Root Mean Squared Error . . . . .	36
DoP	Degree of Polarization . . . . .	51

BINARY CLASSIFICATION OF AN UNKNOWN OBJECT  
THROUGH ATMOSPHERIC TURBULENCE USING A POLARIMETRIC  
BLIND-DECONVOLUTION ALGORITHM AUGMENTED  
WITH ADAPTIVE DEGREE OF LINEAR POLARIZATION PRIORS

## I. Introduction

Polarization is one of the fundamental properties of light along with irradiance, wavelength, and coherence [6]. When scattered light is reflected from an object, its polarization signature provides information about surface features, shape, shading, and roughness [20, 26]. Since human activities often change material surface features, thus affecting the polarization signature of reflected light, polarimetric imaging has emerged as a powerful tool to enhance understanding of an underlying scene of interest. For example, using polarimetric imagery, Wolff presented a material-classification model to accurately discriminate between a dielectric and a metal based on the polarimetric differences in reflecting light at their surfaces [27]. This relatively new polarimetric imaging field has a variety of applications ranging from remote sensing to industrial machine vision systems [26, 27].

Remote sensing refers to the process of acquiring information about an object without physical contact with the object. Remote sensing can be categorized as active or passive depending on the nature of the illumination source. In passive remote sensing, the source of illumination is not controlled, e.g., the sun. An application example of passive remote sensing is the detection of hazardous industrial or warfare chemical agents [2]. On the other hand, active remote sensing uses a controlled source to illuminate the object of interest. Ranging systems such as radio detection and ranging (RADAR) and laser detection and ranging (LADAR) are common examples of active remote sensing systems.

The use of polarimetric imagery has increased the capabilities of passive remote sensing systems, as polarization reveals information largely uncorrelated with spectral and irradiance images [22, 26]. For example, Goudail *et al.* presented polarimetric image processing techniques which show that polarimetric images can improve target detection and segmentation in remote sensing [9]. In addition to Wolff’s early work in polarization-based material classification, Thilak *et al.* introduced a polarization-based approach to estimate the complex index of refraction for characterizing the materials comprising an object [22]. Other studies in material classification are found in [24, 28].

Recently, Hyde developed a variant of the polarimetric blind-deconvolution algorithm presented in [15] for classifying the material of an unknown object using polarimetric imagery degraded by atmospheric turbulence [11]. In his algorithm, prior knowledge about the sought degree of linear polarization (DoLP), called the DoLP prior, serves to classify an object as a metal or a dielectric. Hyde’s algorithm, however, suffers when classifying an object at near-normal collection geometries because of the weak manner in which natural materials polarize light in these conditions. The purpose of this thesis is to present and develop methods to alleviate this limitation.

### **1.1 Goals**

The purpose of this research is to develop an algorithm, somewhat invariant with respect to collection geometry, to discriminate between metals and dielectrics using polarimetric imagery degraded by atmospheric turbulence. The quality of polarimetric information collected by a camera highly relies on geometry. The proposed method enhances the poor performance of the previously developed material-classification algorithm for near-normal collection geometries by adaptively updating the DoLP priors of a metal and a dielectric as more information about the target scene becomes available. The method first recovers the target scene from a set of degraded polarimetric images using the blind-deconvolution technique. Applying the updated DoLP priors, the method then discriminates between metals and dielectrics.

## 1.2 Assumptions

In order to implement the proposed material-classification algorithm, the following assumptions are made about the passive polarimetric remote sensing scenarios modeled in this research.

First, the unknown object in the target scene is assumed to be illuminated with a randomly polarized natural light source, e.g., the sun. Several studies have shown that the circular polarization component of light reflected from an object illuminated with a natural light source is negligible [4, 16, 23]. Thus only the linear components of polarization, i.e., the Stokes parameters  $S_0$ ,  $S_1$ , and  $S_2$ , are considered throughout this research.

Secondly, polarimetric imagery is assumed to be collected in the specular plane. The specular plane is determined by the directions of the incident and reflected light, following the simple geometry of reflection from a smooth (or mirror-like) surface [27]. In passive polarimetry, the angle of polarization (AoP) provides information about the object geometry, and observation made in the specular plane implies that the AoP is zero [11]. As a result, the AoP is not considered in this research, but should be considered in future research on this topic.

The final assumption is that the atmospheric turbulence is relatively weak. In the observation plane, weak atmospheric turbulence randomly changes the light's phase but not its irradiance [7]. Strong atmospheric turbulence, on the other hand, causes phase and irradiance fluctuations, commonly called scintillation [1]. The algorithm presented in this research is designed to correct phase aberrations of degraded images and therefore is only applicable to weak atmospheric turbulence. This is not a very restrictive assumption considering that the light in this analysis is assumed to be spatially incoherent (see assumption 1).



### ***1.3 Thesis Outline***

This thesis consists of five chapters including the introduction. Chapter II provides the theoretical background necessary to understand the development of the material-classification algorithm. The chapter starts with an explanation of polarization and imaging through atmospheric turbulence. A description of the blind-deconvolution method is then followed by a review of the material-classification algorithm in its current form. Chapter III provides detailed descriptions of the novel methods for adaptively updating the DoLP priors in order to alleviate the aforementioned limitation of collection geometry. Chapter IV presents the results of the proposed method using polarimetric imagery obtained at a near-normal collection geometry. Finally, Chapter V summarizes the findings of this research and presents possible topics for future studies.

## II. Background

This chapter provides the background necessary for understanding the polarimetric blind-deconvolution algorithm used for material classification. A brief overview of polarization, incoherent imaging, atmospheric turbulence, and blind deconvolution is presented.

### 2.1 Polarization

*2.1.1 Polarization State.* Polarization simply describes the orientation of the electric field. The electric field  $\mathbf{E}(z, t)$  at any location  $z$  and time  $t$  can be represented by two orthogonal vector components, i.e.,

$$\mathbf{E}(z, t) = \mathbf{E}_x(z, t) + \mathbf{E}_y(z, t) \quad (2.1)$$

where

$$\begin{aligned} \mathbf{E}_x(z, t) &= E_{0x} \cos(\omega t - kz) \\ \mathbf{E}_y(z, t) &= E_{0y} \cos(\omega t - kz - \varepsilon) \end{aligned} \quad (2.2)$$

Here,  $E_{0x}$  and  $E_{0y}$  are the  $x$ - and  $y$ -component amplitudes,  $\omega$  is the angular frequency,  $k$  is the wavenumber, and  $\varepsilon$  is the relative phase difference between the vector components [10, 20]. Equation (2.2) leads to

$$\left(\frac{\mathbf{E}_y}{E_{0y}}\right)^2 + \left(\frac{\mathbf{E}_x}{E_{0x}}\right)^2 - 2\left(\frac{\mathbf{E}_x}{E_{0x}}\right)\left(\frac{\mathbf{E}_y}{E_{0y}}\right)\cos\varepsilon = \sin^2\varepsilon, \quad (2.3)$$

which describes an ellipse rotated through an angle  $\psi$  as shown in Fig. 2.1 [10]. The angle  $\psi$  is called the AoP and is expressed as [20]

$$\tan 2\psi = \frac{2E_{0x}E_{0y}}{E_{0x}^2 - E_{0y}^2} \cos\varepsilon. \quad (2.4)$$

When the relative phase difference  $\varepsilon = \pm\pi/2, \pm3\pi/2, \pm5\pi/2, \dots$ , Eq. (2.3) reduces to

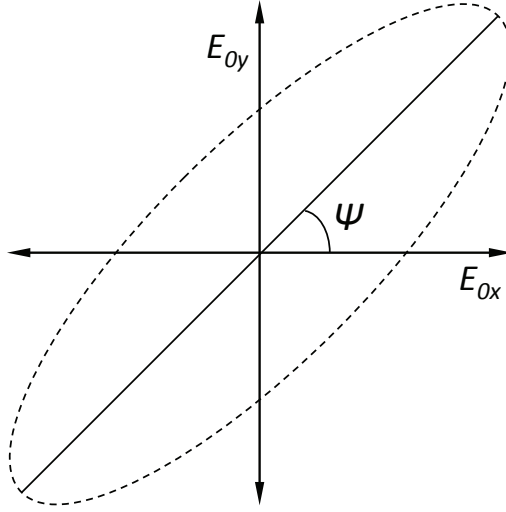


Figure 2.1: Illustration of the polarization ellipse rotated through angle  $\psi$ .

$$\left(\frac{\mathbf{E}_y}{E_{0y}}\right)^2 + \left(\frac{\mathbf{E}_x}{E_{0x}}\right)^2 = 1, \quad (2.5)$$

which describes an ellipse in which the major and minor axes are aligned with the  $x$  and  $y$  axes. The resultant electric field vector  $\mathbf{E}(z, t)$  will appear to rotate and change its amplitude as it propagates. Light in this state is called elliptically polarized light. Elliptical polarization is the most general polarization state of light.

In the case that the  $x$ - and  $y$ -component amplitudes are equal, i.e.,  $E_{0x} = E_{0y} = E_0$ , Eq. (2.5) further reduces to

$$(\mathbf{E}_y)^2 + (\mathbf{E}_x)^2 = E_0^2 \quad (2.6)$$

yielding circularly polarized light [10]. If the relative phase difference  $\varepsilon = 0, \pm\pi, \pm2\pi, \dots$ , Eq. (2.3) becomes

$$\mathbf{E}_y = \pm \frac{E_{0y}}{E_{0x}} E_{0x}, \quad (2.7)$$

which is the equation of a line with slope  $\pm E_{0y}/E_{0x}$ . Light in this state is called linearly polarized light [10].

*2.1.2 Stokes Vectors and Mueller Matrices.* One problem with modeling polarization using the polarization ellipse formulation is that it is limited to scenarios involving fully polarized light. Stokes vectors overcome this limitation by describing polarization in terms of observable quantities, namely, optical power or irradiance [20]. By taking time averages of the electric field vector components, Eq. (2.3) can be shown to yield

$$S_0^2 = S_1^2 + S_2^2 + S_3^2, \quad (2.8)$$

where

$$\begin{aligned} S_0 &= E_{0x}^2 + E_{0y}^2 \\ S_1 &= E_{0x}^2 - E_{0y}^2 \\ S_2 &= 2E_{0x}E_{0y} \cos \varepsilon \\ S_3 &= 2E_{0x}E_{0y} \sin \varepsilon \end{aligned} \quad (2.9)$$

The parameter  $S_0$  is the total irradiance. The parameter  $S_1$  is the difference in the irradiance of light passed by a horizontal linear polarizer and a vertical linear polarizer. If  $S_1 = 0$ , light may be linearly or elliptically polarized at  $\pm 45^\circ$ , circularly polarized, or unpolarized [10]. The parameter  $S_2$  is the difference in the irradiance of light passed by a linear polarizer at  $+45^\circ$  and a linear polarizer at  $-45^\circ$ . Finally, the parameter  $S_3$  is the difference in the irradiance of light passed by a right-handed circular polarizer and a left-handed circular polarizer. The Stokes parameters are often represented in a normalized column vector as

$$\mathbf{S} = S_0 \begin{bmatrix} 1 & S_1/S_0 & S_2/S_0 & S_3/S_0 \end{bmatrix}^T. \quad (2.10)$$

The Mueller matrix is a  $4 \times 4$  matrix which models the polarization effects of an optical interaction [20]. It relates the Stokes vector incident on an optical element  $\mathbf{S}^{\text{in}}$  to the Stokes vector leaving the element  $\mathbf{S}^{\text{out}}$  as

$$\mathbf{S}^{\text{out}} = \mathbf{M}\mathbf{S}^{\text{in}}$$

$$\begin{bmatrix} S_0^{\text{out}} \\ S_1^{\text{out}} \\ S_2^{\text{out}} \\ S_3^{\text{out}} \end{bmatrix} = \begin{bmatrix} m_{00} & m_{01} & m_{02} & m_{03} \\ m_{10} & m_{11} & m_{12} & m_{13} \\ m_{20} & m_{21} & m_{22} & m_{23} \\ m_{30} & m_{31} & m_{32} & m_{33} \end{bmatrix} \begin{bmatrix} S_0^{\text{in}} \\ S_1^{\text{in}} \\ S_2^{\text{in}} \\ S_3^{\text{in}} \end{bmatrix} \quad (2.11)$$

where  $\mathbf{M}$  is the Mueller matrix of the optical element [20]. For example, the polarization effect on light passing through an ideal linear polarizer oriented at an angle  $\theta$  from the horizontal is expressed as

$$\mathbf{S}^{\text{out}} = \mathbf{M}_\theta \mathbf{S}^{\text{in}}$$

$$\begin{bmatrix} S_0^{\text{out}} \\ S_1^{\text{out}} \\ S_2^{\text{out}} \\ S_3^{\text{out}} \end{bmatrix} = \frac{1}{2} \begin{bmatrix} 1 & \cos 2\theta & \sin 2\theta & 0 \\ \cos 2\theta & \cos^2 2\theta & \sin 2\theta \cos 2\theta & 0 \\ \sin 2\theta & \sin 2\theta \cos 2\theta & \sin^2 2\theta & 0 \\ 0 & 0 & 0 & 0 \end{bmatrix} \begin{bmatrix} S_0^{\text{in}} \\ S_1^{\text{in}} \\ S_2^{\text{in}} \\ S_3^{\text{in}} \end{bmatrix} \quad (2.12)$$

$$= \frac{1}{2} \begin{bmatrix} S_0^{\text{in}} + S_1^{\text{in}} \cos 2\theta + S_2^{\text{in}} \sin 2\theta \\ S_0^{\text{in}} \cos 2\theta + S_1^{\text{in}} \cos^2 2\theta + S_2^{\text{in}} \sin 2\theta \cos 2\theta \\ S_0^{\text{in}} \sin 2\theta + S_1^{\text{in}} \sin 2\theta \cos 2\theta + S_2^{\text{in}} \sin^2 2\theta \\ 0 \end{bmatrix}$$

Since incident light is filtered through a linear polarizer, Eq. (2.12) shows that the  $S_3$  component of the output Stokes vector (the term describing the amount of circularly polarized light) is zero. The total irradiance passed by the linear polarizer is contained in the  $S_0$  component of the output Stokes vector. Therefore, the irradiance  $I(\theta)$  measured by a detector with an ideal polarizer oriented at an angle  $\theta$  is given by

$$I(\theta) = S_0^{\text{out}} = \frac{1}{2}(S_0^{\text{in}} + S_1^{\text{in}} \cos 2\theta + S_2^{\text{in}} \sin 2\theta). \quad (2.13)$$

Equation (2.13) is an important result and used in the polarimetric blind-deconvolution algorithm discussed in Section 2.5.

As mentioned in Chapter 1, it is assumed that the contribution from circular polarization is not significant in this research. Therefore, the full Stokes vector can be simplified to the linear-polarization-state Stokes vector, eliminating the parameter  $S_3$  whose value is approximately zero for the cases of interest here. The AoP  $\psi$  introduced in Eq. (2.4) can be expressed in terms of the Stokes parameters as [20]

$$\tan 2\psi = \frac{2E_{0x}E_{0y}}{E_{0x}^2 - E_{0y}^2} \cos \varepsilon = \frac{S_2}{S_1}. \quad (2.14)$$

Like the AoP, the DoLP can be obtained from knowledge of the Stokes parameters as well:

$$\text{DoLP} = \frac{I_{\text{pol}}}{I_{\text{tot}}} = \frac{\sqrt{S_1^2 + S_2^2}}{S_0} \quad (2.15)$$

where  $I_{\text{pol}}$  is the linearly polarized light irradiance and  $I_{\text{tot}}$  is the total irradiance. Its range is between 0, i.e., randomly or unpolarized state, and 1, fully polarized.

## 2.2 Imaging

*2.2.1 Incoherent Imaging.* Incoherent illumination implies that each spatial point on the object field is statistically independent of all other points [18]. In the case of incoherent imaging, the image irradiance  $i(x, y)$  can be found by convolving the object irradiance  $o(x, y)$  and the irradiance impulse response of the optical path of interest, also known as the point spread function (PSF)  $|h(x, y)|^2$ :

$$i(x, y) = \int \int_{-\infty}^{\infty} |h(x - u, y - v)|^2 o(u, v) du dv \quad (2.16)$$

where  $(x, y)$  defines an image plane coordinate and  $(u, v)$  defines an object/target plane coordinate. Note that because of the nature of imaging  $(u, v)$  and  $(x, y)$  are typically related by the magnification  $M$ . Without loss of generality, unit magnification is assumed in all analysis to follow. Taking the Fourier transform of Eq. (2.16) gives the equivalent relationship of incoherent imaging in the spatial-frequency domain as

$$I(f_x, f_y) = H(f_x, f_y)O(f_x, f_y) \quad (2.17)$$

where  $I(f_x, f_y)$ ,  $O(f_x, f_y)$ , and  $H(f_x, f_y)$  are the Fourier transforms of  $i(x, y)$ ,  $o(x, y)$ , and  $|h(x, y)|^2$ , respectively, and  $(f_x, f_y)$  is the spatial-frequency coordinate corresponding to the image-plane coordinate  $(x, y)$  [8]. Normalizing  $H(f_x, f_y)$  by its value at zero frequency yields the function  $\mathcal{H}$  [8]:

$$\mathcal{H}(f_x, f_y) = \frac{\int \int_{-\infty}^{\infty} |h(x, y)|^2 \exp[-j2\pi(f_x x + f_y y)] dx dy}{\int \int_{-\infty}^{\infty} |h(x, y)|^2 dx dy}. \quad (2.18)$$

The function  $\mathcal{H}$  is called the optical transfer function (OTF), and its modulus  $|\mathcal{H}|$  is referred to as the modulation transfer function (MTF), commonly used to characterize imaging systems.

*2.2.2 The OTF of a Diffraction-Limited Incoherent Imaging System.* An optical system is said to be diffraction limited if an image is limited in quality only by diffraction, not by imperfections in the imaging system [8]. The OTF of a diffraction-limited incoherent imaging system with a circular aperture of diameter  $D$  is given by [8]

$$\mathcal{H}(\rho) = \begin{cases} \frac{2}{\pi} \left[ \cos^{-1} \left( \frac{\rho}{2\rho_0} \right) - \left( \frac{\rho}{2\rho_0} \right) \sqrt{1 - \left( \frac{\rho}{2\rho_0} \right)^2} \right] & \text{if } \rho \leq 2\rho_0 \\ 0 & \text{otherwise} \end{cases}, \quad (2.19)$$

where  $\rho_0$  is the cutoff frequency of a coherent imaging system of focal length  $f$  and wavelength  $\lambda$ , i.e.,

$$\rho_0 = \frac{D}{2\lambda f}. \quad (2.20)$$

The range of the radial distance  $\rho = \sqrt{f_x^2 + f_y^2}$  in Eq. (2.19) indicates that an incoherent imaging system extends the cutoff frequency to twice that of a coherent imaging system [8].

*2.2.3 Atmospheric Turbulence.* Atmospheric turbulence is predominantly caused by temperature fluctuations in the atmosphere resulting from differential heating and cooling of Earth's surface by the sun [18]. These temperature fluctuations cause spatial and temporal fluctuations in the index of refraction of the atmosphere resulting in random spatial and temporal variations in optical path length (OPL) experienced by transiting light [18]. These OPL variations manifest phase aberrations in the optical wavefront as the light propagates through the atmosphere. These phase aberrations add another layer of distortion in addition to the imaging system. As a result, the quality of received images is degraded and the resolution of the imaging system is reduced.

*2.2.4 Imaging through Turbulence.* The instantaneous PSF and its OTF through atmospheric turbulence are random due to the stochastic nature of the atmosphere, as described above [18]. Physical meaning can only be gleaned by inspection of the average PSF and its Fourier transform, the average OTF. To see how atmospheric phase aberrations are modeled using the OTF  $\mathcal{H}$ , Eq. (2.18) is first expressed in a different form [7, 8]:

$$\mathcal{H}(f_x, f_y) = \frac{\int \int_{-\infty}^{\infty} H(x, y) H^*(x - \lambda f f_x, y - \lambda f f_y) dx dy}{\int \int_{-\infty}^{\infty} |H(x, y)|^2 dx dy}. \quad (2.21)$$

Here, the function  $H$  represents a modified aperture function, i.e.,



$$H(x, y) = P(x, y)t(x, y) \quad (2.22)$$

where  $P(x, y)$  is the classic aperture apodization function and  $t(x, y)$  is the complex transmittance given by

$$t(x, y) = \exp[j\theta(x, y)]. \quad (2.23)$$

In Eq. (2.23),  $\theta(x, y)$  represents the random phase induced by the atmosphere [7]. Substituting Eq. (2.22) into Eq. (2.21) yields an expression for the instantaneous OTF of an imaging system including atmospheric effects  $\mathcal{H}_{sys}$  [7]:

$$\mathcal{H}_{sys}(f_x, f_y) = \frac{\int \int_{-\infty}^{\infty} P(x, y)P^*(x - \lambda f f_x, y - \lambda f f_y)t(x, y)t^*(x - \lambda f f_x, y - \lambda f f_y)dx dy}{\int \int_{-\infty}^{\infty} |P(x, y)|^2 dx dy}. \quad (2.24)$$

The average OTF of the imaging system  $\bar{\mathcal{H}}_{sys}(f_x, f_y)$  is computed by taking the expectation of Eq. (2.24) yielding

$$\bar{\mathcal{H}}_{sys}(f_x, f_y) = \frac{\int \int_{-\infty}^{\infty} P(x, y)P^*(x - \lambda f f_x, y - \lambda f f_y)E[t(x, y)t^*(x - \lambda f f_x, y - \lambda f f_y)] dx dy}{\int \int_{-\infty}^{\infty} |P(x, y)|^2 dx dy}. \quad (2.25)$$

Equation (2.25) can be written as

$$\bar{\mathcal{H}}_{sys}(f_x, f_y) = \mathcal{H}_O(f_x, f_y) \bar{\mathcal{H}}_S(f_x, f_y), \quad (2.26)$$

where  $\mathcal{H}_O(f_x, f_y)$  is the OTF of a diffraction-limited system and  $\bar{\mathcal{H}}_S(f_x, f_y)$  represents the average OTF of the induced random phase [7]. Two types of the average OTF are discussed in this section—long-exposure and short-exposure OTFs.

Long-exposure imaging is imaging performed over a long integration time. Because of the long integration time, many instances/realizations of atmospheric turbulence are captured in the resulting image. The long-exposure OTF of the atmosphere was derived by Fried as

$$\bar{\mathcal{H}}_{LE}(\rho) = \exp \left[ -3.44 \left( \frac{\lambda f \rho}{r_0} \right) \right] \quad (2.27)$$

where  $r_0$  is the atmospheric coherence diameter [19]. The atmospheric coherence diameter describes the largest effective aperture diameter for image resolution. For a plane wave source,  $r_0$  can be computed as

$$r_{0,pw} = \left[ 0.423 k^2 \int_0^L C_n^2(z) dz \right]^{-3/5} \quad (2.28)$$

where  $C_n^2$  is the refractive-index structure parameter, which is a measure of the turbulence strength, and  $L$  is the propagation distance [19].

Short-exposure imaging is imaging performed over a short integration time. In short-exposure imaging, only a single instance of atmospheric turbulence is captured in the image thus effectively freezing the effects of the atmosphere [18]. The key difference between short-exposure and long-exposure imaging is that images taken using a short exposure are not distorted by wavefront tilt which has the effect of broadening the PSF (or equivalently narrowing the OTF) in the long-exposure case [18]. The short-exposure OTF of the atmosphere is given by

$$\bar{\mathcal{H}}_{SE}(\rho) = \exp \left\{ -3.44 \left( \frac{\lambda f \rho}{r_0} \right)^{5/3} \left[ 1 - \alpha \left( \frac{\lambda f \rho}{D} \right) \right]^{1/3} \right\} \quad (2.29)$$

where  $\alpha$  is 1/2 or 1 when scintillation is or is not present, respectively [19]. Note that  $\bar{\mathcal{H}}_{SE}$  reduces to  $\bar{\mathcal{H}}_{LE}$  by setting  $\alpha = 0$ . Figure 2.2 illustrates how atmospheric turbulence corrupts an image and reduces the resolution of an imaging system as compared to the diffraction-limited case.

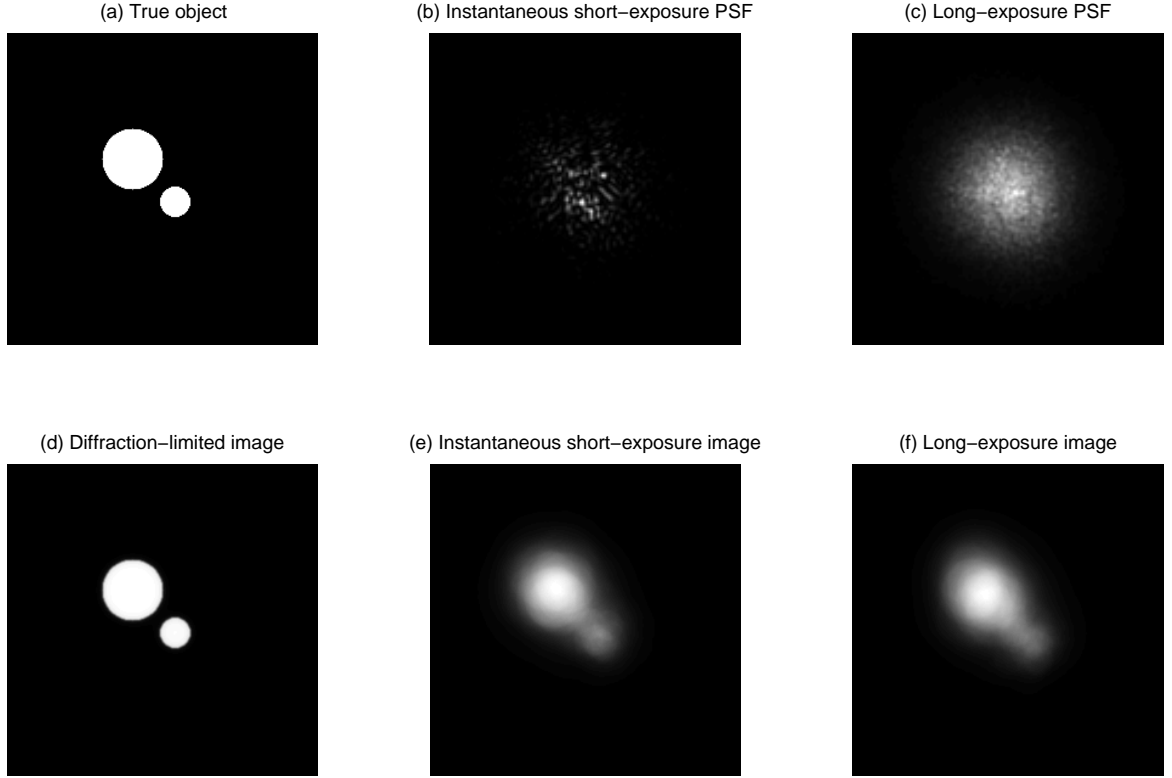


Figure 2.2: Effect of atmospheric turbulence on imaging.

### 2.3 *Blind Deconvolution*

Blind deconvolution refers to the process of estimating the true object and the PSF from degraded images with no or partial information about the imaging system or object [14]. Blind deconvolution has applications in various fields including optics, astronomy, signal processing, and seismology. There exist many methods to solve the blind-deconvolution problem, such as zeros sheet separation, *a priori* blur identification, parametric estimation, etc. [14]. Among these approaches, the most relevant to this thesis is the maximum-likelihood (ML) estimation method, which is a parametric estimation technique. ML blind-deconvolution algorithms developed by Schultz and LeMaster and Cain will be summarized here after a brief review of ML estimation.

*2.3.1 Maximum-Likelihood Estimation.* The ML method solves a blind-deconvolution problem by estimating the parameter set  $\boldsymbol{\theta} = [\theta_1, \theta_2, \dots, \theta_N]^T$  of a distribution  $X$  based on the observed data  $\mathbf{x} = [x_1, x_2, \dots, x_N]^T$  drawn according to the distribution  $X$  [17]. An estimate of the parameters is made to maximize the probability or likelihood of observing data  $\mathbf{x}$  given the parameter set  $\boldsymbol{\theta}$  [14]. Let  $f(\mathbf{x}|\boldsymbol{\theta})$  be the conditional probability density function (PDF) of the distribution  $X$  given the parameter set  $\boldsymbol{\theta}$  [17]. The ML estimate of  $\boldsymbol{\theta}$  is then

$$\hat{\boldsymbol{\theta}}_{ml} = \arg \left\{ \max_{\boldsymbol{\theta}} l_{\mathbf{x}}(\boldsymbol{\theta}) \right\} = \arg \left\{ \max_{\boldsymbol{\theta}} f(\mathbf{x}|\boldsymbol{\theta}) \right\}, \quad (2.30)$$

where  $l_{\mathbf{x}}(\boldsymbol{\theta})$  denotes the likelihood function [14]. Since most distributions of engineering interest belong to the exponential family such as Gaussian, Rayleigh, Poisson, etc., the logarithm of the likelihood function is often utilized in Eq. (2.30) [17]. Note that the logarithm is a monotone function, thus maximizing the log-likelihood function is equivalent to maximizing the likelihood [17]:

$$L(\boldsymbol{\theta}) = \log l_{\mathbf{x}}(\boldsymbol{\theta}) = \log f(\mathbf{x}|\boldsymbol{\theta}). \quad (2.31)$$

*2.3.2 Expectation-Maximization Algorithm.* The expectation-maximization (EM) algorithm is an iterative algorithm to produce ML estimates of the parameter set  $\boldsymbol{\theta}$ . In the EM algorithm, the observed/measured data  $\mathbf{y} = [y_1, y_2, \dots, y_N]^T$ , termed the incomplete data, is mapped to a new set of data  $\mathbf{x} = [x_1, x_2, \dots, x_N]^T$ , termed the complete data, where the ML estimation problem is more easily solved [21]. Note that the complete data  $\mathbf{x}$  are not observed directly and thus do not need to have a physical meaning. They only need to be statistically consistent with the incomplete data  $\mathbf{y}$  [15]. The idea behind the EM algorithm is that even though the complete data specification is not known, making use of the underlying distribution  $\log[f(\mathbf{x}|\boldsymbol{\theta})]$ , an estimate of  $\boldsymbol{\theta}$  can be determined [17]. Obtaining this estimate  $\hat{\boldsymbol{\theta}}_{ml}$  is a nonlinear optimization problem of several variables [14]. Among various implementation methods, the EM

algorithm is the most popular for its simplicity and computational efficiency [14]. The EM algorithm converts the nonlinear optimization problem into a simpler linear iterative procedure, making implementation straightforward.

The goal of the EM algorithm is to find the parameter set  $\boldsymbol{\theta}$  which maximizes the log-likelihood  $\log[f(\mathbf{x}|\boldsymbol{\theta})]$  [17]. Recall that the complete data  $\mathbf{x}$  are not directly observed and thus it is not possible to compute the log-likelihood of  $\mathbf{x}$  directly [17]. Instead, the EM algorithm maximizes the expectation of  $\log[f(\mathbf{x}|\boldsymbol{\theta})]$  given the incomplete data  $\mathbf{y}$  and the current estimate of the parameter set  $\boldsymbol{\theta}$  [17]. The expectation step (the first step of the EM algorithm) computes this conditional expectation, i.e.,

$$Q(\boldsymbol{\theta}|\boldsymbol{\theta}^k) = E [\log f(\mathbf{x}|\boldsymbol{\theta})|\mathbf{y}, \boldsymbol{\theta}^k] \quad (2.32)$$

where  $Q(\boldsymbol{\theta}|\boldsymbol{\theta}^k)$  is called the objective function and  $\boldsymbol{\theta}^k$  represents the estimate of  $\boldsymbol{\theta}$  after  $k$  iterations [17]. Once the objective function  $Q$  is defined, the maximization step (the second step of the EM algorithm) provides a new estimate of the parameter set  $\boldsymbol{\theta}^{k+1}$  by maximizing  $Q$  [17],

$$\boldsymbol{\theta}^{k+1} = \arg \left\{ \max_{\boldsymbol{\theta}} Q(\boldsymbol{\theta}|\boldsymbol{\theta}^k) \right\}. \quad (2.33)$$

The EM algorithm starts with choosing an initial  $\boldsymbol{\theta}$  estimate and then is iterated until convergence or a stopping criterion is met.

## 2.4 *Multiframe Blind-Deconvolution*

Unconstrained ML estimation, discussed in Section 2.3, can converge to a trivial solution, namely, the object is estimated as a point source and the PSF is estimated as the measured data. This estimate needs to be avoided because it provides no information about the true object [21]. Schulz introduces two techniques for performing ML blind deconvolution of a sequence of short-exposure images while avoiding the trivial solution [21]. The first method, penalized ML estimation, adds a penalty term

to the original log-likelihood function so that point-source-like object estimates are penalized [21]. The second proposed method, which is applicable to this research, performs ML blind deconvolution using a parameterized form of the PSF [21]. This approach is described in more detail below.

Let  $o(\mathbf{x})$  and  $h_k(\mathbf{y}|\mathbf{x})$  denote the object's irradiance and the PSF for the  $k^{\text{th}}$  short-exposure image, respectively. The coordinate  $\mathbf{x} = (x_1, x_2)$  defines a point in the object/target plane; the coordinate  $\mathbf{y} = (y_1, y_2)$  defines a point in the image plane [11, 21]. Assuming discretized object and image plane regions, the ideal irradiance in the  $k^{\text{th}}$  frame is

$$i_k(\mathbf{y}; o, h_k) = \sum_{\mathbf{x}} h_k(\mathbf{y}|\mathbf{x}) o(\mathbf{x}). \quad (2.34)$$

This ideal irradiance is never actually measured. What is actually detected is a noise-degraded version of  $i_k$ . The assumption of this algorithm and the other blind-deconvolution algorithms to follow is that shot noise is the dominant noise source degrading  $i_k$ . Let  $d_k(\mathbf{y})$  be defined as the data detected at location  $\mathbf{y}$  in the  $k^{\text{th}}$  frame where  $i_k(\mathbf{y}; o, h_k) = E[d_k(\mathbf{y})]$ . Since shot noise is Poisson distributed, the log-likelihood  $L(o, h)$  becomes

$$L(o, h) = \sum_k \left[ - \sum_{\mathbf{y}} i_k(\mathbf{y}; o, h_k) + \sum_{\mathbf{y}} d_k(\mathbf{y}) \ln i_k(\mathbf{y}; o, h_k) \right] \quad (2.35)$$

after eliminating terms that do not affect the maximization [21]. The PSF is parameterized by phase errors over the aperture as

$$h_k(\mathbf{y}|\mathbf{x}; \alpha_k, \theta_k) = \alpha_k g(\mathbf{y} - \mathbf{x}; \theta_k), \quad (2.36)$$

where

$$g(\mathbf{x}; \theta_k) = \left| \sum_{\mathbf{u}} A(\mathbf{u}) \exp[i\theta_k(\mathbf{u})] \exp(-i2\pi\kappa\mathbf{u} \cdot \mathbf{x}) \right|^2, \quad (2.37)$$

$A(\mathbf{u})$  is the aperture function,  $\mathbf{u}$  denotes a spatial coordinate pair in the pupil plane,  $\alpha_k$  is the gain of the  $k^{\text{th}}$  PSF,  $\theta_k$  models the phase aberrations caused by atmospheric turbulence or the image system in the  $k^{\text{th}}$  frame, and  $\kappa$  is a scaling constant between pupil-plane and image-plane coordinates [21].

The EM algorithm is then used to optimize estimates of the object irradiance and the parameters  $\alpha_k, \theta_k$ . Substitution of Eqs. (2.34) and (2.36) into Eq. (2.35), the log likelihood becomes

$$\begin{aligned} L(o, h) = & - \sum_k \sum_{\mathbf{y}} \sum_{\mathbf{x}} \alpha_k g(\mathbf{y} - \mathbf{x}; \theta_k) o(\mathbf{x}) + \sum_k \sum_{\mathbf{y}} d_k(\mathbf{y}) \ln \alpha_k \\ & + \sum_k \sum_{\mathbf{y}} d_k(\mathbf{y}) \ln \left[ \sum_{\mathbf{x}} g(\mathbf{y} - \mathbf{x}; \theta_k) o(\mathbf{x}) \right]. \end{aligned} \quad (2.38)$$

The ML estimate of  $\alpha_k$  can be obtained by differentiating Eq. (2.38) with respect to  $\alpha_k$  and setting the derivative to zero [21]. The resulting estimate  $\hat{\alpha}_k$  is

$$\hat{\alpha}_k = D_k / G, \quad (2.39)$$

where  $D_k = \sum_{\mathbf{y}} d_k(\mathbf{y})$  and  $G = \sum_{\mathbf{x}} g(\mathbf{x}; \theta_k)$  [21]. The update equations for the object irradiance  $o(\mathbf{x})$  and the phase parameter  $\theta_k$  are derived by applying the method of Lagrange multipliers and the Gerchberg-Saxton algorithm, respectively:

$$o^{new}(\mathbf{x}) = D^{-1} o^{old}(\mathbf{x}) \sum_k \sum_{\mathbf{y}} \frac{\hat{\alpha}_k g(\mathbf{y} - \mathbf{x}; \theta_k^{old})}{i_k(\mathbf{y}; o^{old}, h_k^{old})} d_k(\mathbf{y}) \quad (2.40)$$

and

$$\theta_k^{new}(u) = \begin{cases} \tilde{\theta}(u) & \text{if } \sum_{\mathbf{x}} \xi(\mathbf{x}; \theta_k^{old}) \ln g(\mathbf{x}; \tilde{\theta}) \geq \sum_{\mathbf{x}} \xi(\mathbf{x}; \theta_k^{old}) \ln g(\mathbf{x}; \theta_k^{old}) \\ \theta_k^{old}(u) & \text{else} \end{cases}, \quad (2.41)$$

where

$$\begin{aligned} \tilde{\theta}(u) &= \text{phase} \left( F_u^{-1} \left\{ \sqrt{\xi(\mathbf{x}; \theta_k^{old})} \exp [i \text{phase} \{ \tilde{g}(\mathbf{x}; \theta_k^{old}) \}] \right\} \right) \\ \xi(\mathbf{x}; \theta_k^{old}) &= g(\mathbf{x}; \theta_k^{old}) \left[ \sum_{\mathbf{y}} \frac{o^{old}(\mathbf{y} - \mathbf{x})}{i_k(\mathbf{y}; o^{old}, h_k^{old})} d_k(\mathbf{y}) \right] \\ \tilde{g}(\mathbf{x}; \theta_k^{old}) &= F_x \{ A(u) \exp [i \theta_k^{old}(u)] \} \end{aligned} \quad (2.42)$$

Here,  $F_x$  denotes a discrete Fourier transform [21]. Figure 2.3 depicts the ML estimation results using Schulz's algorithm just described. The first row of Fig. 2.3 is the true object. The second row shows the two short-exposure PSFs used in this simulation ( $D/r_0 = 20$ ). The third row contains the detected images, which are corrupted by atmospheric turbulence and simulated shot noise (signal-to-noise ratio (SNR) =  $\sqrt{1000}$ ). The fourth row is the estimated object after 200 iterations. The significance of the result is that the object estimate clearly indicates two distinct objects of different sizes. On the contrary, this information is partly lost in the detected images.

## 2.5 Multichannel Blind Deconvolution of Polarimetric Imagery

Recently, LeMaster and Cain developed a polarimetric version of Schulz's polarization insensitive algorithm. In their study, the linear polarization state is considered, and the images, measured by detectors at different polarization orientations (channels), are fused to provide polarimetric information about the scene, namely estimates of the AoP as well as estimates of the object and the channel PSFs [15].



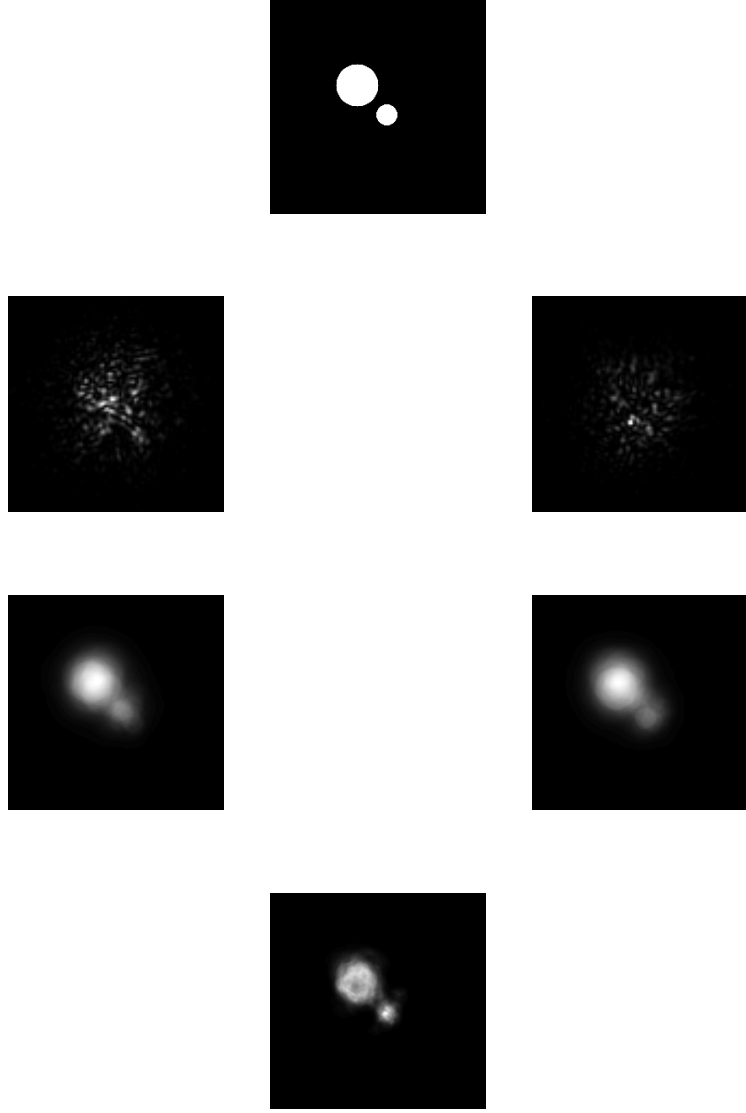


Figure 2.3: ML estimation results using Schulz's parameterized-PSF blind-deconvolution algorithm. The first row is the true object. The second row contains the two short-exposure PSFs used in this simulation ( $D/r_0 = 20$ ). The third row shows the detected images ( $\text{SNR} = \sqrt{1000}$ ). The fourth row is the estimated object after 200 iterations.

As reviewed in Section 2.1.2, the irradiance measured at a detector with a linear polarizer orientated at angle  $\theta$  is given by

$$I(\theta) = \frac{1}{2} (S_0 + S_1 \cos 2\theta + S_2 \sin 2\theta) \quad (2.43)$$

where

$$\begin{aligned} S_1 &= PS_0 \cos 2\alpha \\ S_2 &= PS_0 \sin 2\alpha \end{aligned} \quad (2.44)$$

Here,  $\alpha$  is the AoP and  $P$  is the DoLP. Substitution of Eq. (2.44) into Eq. (2.43) and subsequent simplification yields

$$o_c(\mathbf{x}) = \frac{1}{2}\lambda_u(\mathbf{x}) + \lambda_p(\mathbf{x})\cos^2(\alpha(\mathbf{x}) - \theta_c). \quad (2.45)$$

where  $\lambda_u = (1 - P)S_0$  and  $\lambda_p = PS_0$  represent the unpolarized and polarized components of the scene, respectively [15]. Given the PSF  $h_c$  and the object irradiance  $o_c$ , the ideal irradiance  $i_c$  is

$$i_c(\mathbf{y}) = \sum_{\mathbf{x}} o_c(\mathbf{x})h_c(\mathbf{y} - \mathbf{x}). \quad (2.46)$$

As in Schulz's algorithm, the incomplete data  $d_c(\mathbf{y})$  denote the number of photons at location  $\mathbf{y}$  in polarization channel  $c$ . Each  $d_c$  is subsequently split into polarized and unpolarized components  $\tilde{d}_{pc}(\mathbf{y}, \mathbf{x})$  and  $\tilde{d}_{uc}(\mathbf{y}, \mathbf{x})$ , which in accordance with the dictates of the EM algorithm become the complete data:

$$d_c(\mathbf{y}) = \sum_{\mathbf{x}} \tilde{d}_{uc}(\mathbf{y}, \mathbf{x}) + \sum_{\mathbf{x}} \tilde{d}_{pc}(\mathbf{y}, \mathbf{x}) \quad (2.47)$$

where

$$\begin{aligned} E[\tilde{d}_{pc}(\mathbf{y}, \mathbf{x})] &= \frac{1}{2}\lambda_u(\mathbf{x}) \\ E[\tilde{d}_{uc}(\mathbf{y}, \mathbf{x})] &= \lambda_p(\mathbf{x})\cos^2(\alpha(\mathbf{x}) - \theta_c) \end{aligned} \quad (2.48)$$

Substituting Eqs. (2.45)–(2.47) into Eq. (2.35), the complete data log-likelihood function  $L^{CD}$  becomes [15]

$$\begin{aligned}
L^{CD}(\lambda_u, \lambda_p, \alpha, h) = & \sum_c \sum_{\mathbf{y}} \sum_{\mathbf{x}} \left\{ \tilde{d}_{uc}(\mathbf{y}, \mathbf{x}) \ln \left[ \frac{1}{2} \lambda_u(\mathbf{x}) h_c(\mathbf{y} - \mathbf{x}) \right] - \frac{1}{2} \lambda_u(\mathbf{x}) h_c(\mathbf{y} - \mathbf{x}) \right\} \\
& + \sum_c \sum_{\mathbf{y}} \sum_{\mathbf{x}} \left\{ \tilde{d}_{pc}(\mathbf{y}, \mathbf{x}) \ln [\lambda_p(\mathbf{x}) \cos^2(\alpha(\mathbf{x}) - \theta_c) h_c(\mathbf{y} - \mathbf{x})] \right. \\
& \quad \left. - \lambda_p(\mathbf{x}) \cos^2(\alpha(\mathbf{x}) - \theta_c) h_c(\mathbf{y} - \mathbf{x}) \right\}
\end{aligned} \tag{2.49}$$

Update equations for the sought parameters are obtained by calculating the conditional expectation of  $L^{CD}$  (expectation step) and maximizing the resulting expression for  $\lambda_u(\mathbf{x})$ ,  $\lambda_p(\mathbf{x})$ ,  $\alpha(\mathbf{x})$ , and  $h_c(\mathbf{y}|\mathbf{x})$ . The resulting update equations for the polarization components  $\lambda_u$  and  $\lambda_p$  at pixel  $\mathbf{x}_0$  are [15]

$$\lambda_k^{n+1}(\mathbf{x}_0) = \frac{2}{C} \sum_c \sum_{\mathbf{y}} \psi_{kc}^{n+1}(\mathbf{y}, \mathbf{x}_0), \tag{2.50}$$

where  $k$  refers to either  $u$  or  $p$  for the unpolarized or polarized component, respectively,  $C$  is the number of channels, and

$$\begin{aligned}
\psi_{pc}^{n+1}(\mathbf{y}, \mathbf{x}) &= \frac{d_c(\mathbf{y})}{i_c^n(\mathbf{y})} \lambda_p^n(\mathbf{x}) \cos^2(\alpha^n(\mathbf{x}) - \theta_c) h_c^n(\mathbf{y} - \mathbf{x}) \\
\psi_{uc}^{n+1}(\mathbf{y}, \mathbf{x}) &= \frac{1}{2} \frac{d_c(\mathbf{y})}{i_c^n(\mathbf{y})} \lambda_u(\mathbf{x}) h_c(\mathbf{y} - \mathbf{x})
\end{aligned} \tag{2.51}$$

The AoP estimate is [15]

$$\alpha^{n+1}(\mathbf{x}_0) = \frac{1}{2} \tan^{-1} \frac{S_2^{n+1}(\mathbf{x}_0)}{S_1^{n+1}(\mathbf{x}_0)}. \tag{2.52}$$

Finally, the PSF is estimated according to the update equations introduced by Schulz [Eqs. (2.36), (2.37), (2.41), and (2.42)], where the gain  $\alpha_k$  is set to unity such that

$$h_k(\mathbf{y}|\mathbf{x}; \alpha_k, \theta_k) = g(\mathbf{y} - \mathbf{x}; \theta_k). \tag{2.53}$$

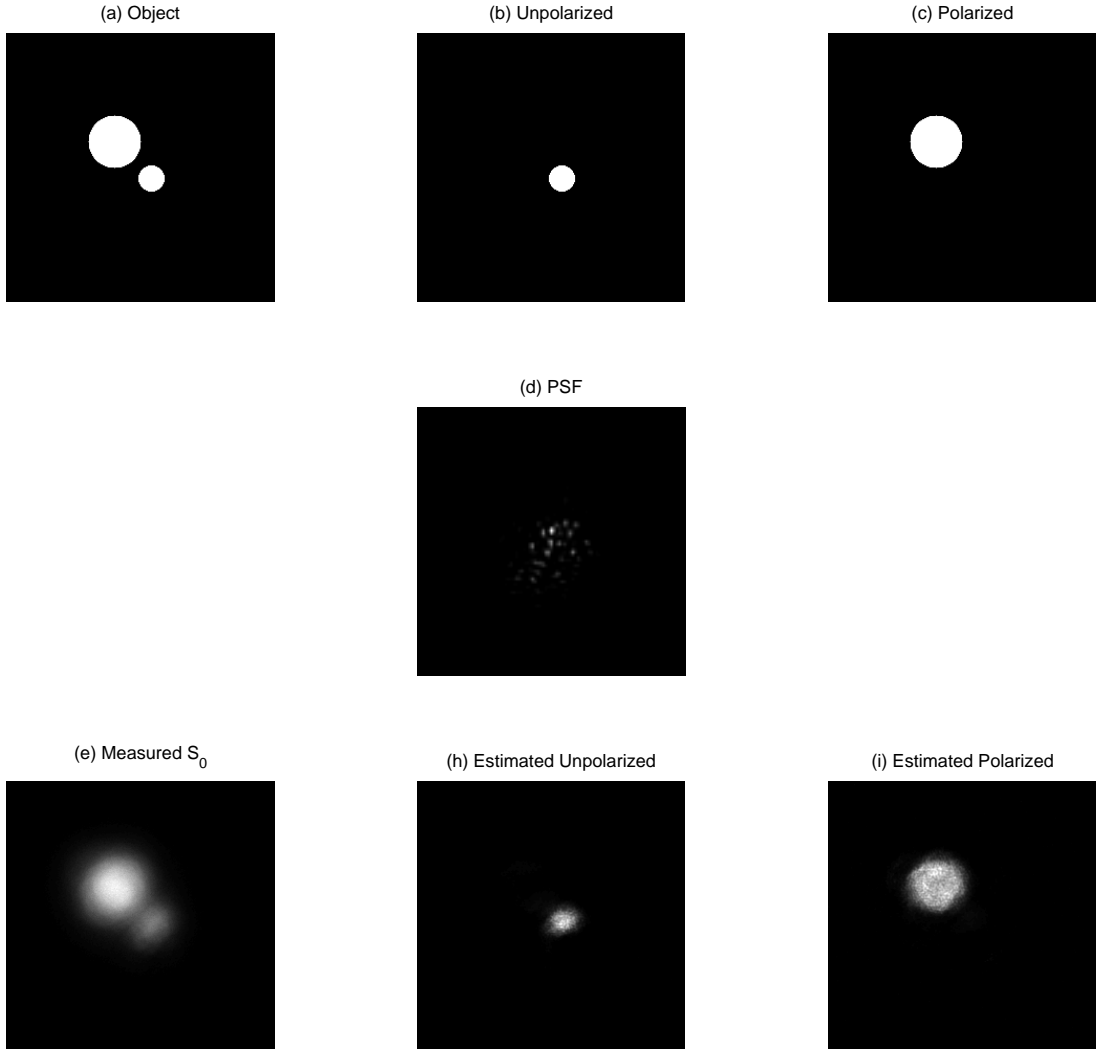


Figure 2.4: ML estimation results using three-channel ( $0^\circ, 60^\circ, 120^\circ$ ) polarimetric imagery. The first row contains the true object and its unpolarized and polarized components. The second row depicts the simulated short-exposure PSF ( $D/r_0 = 20$ ). Shown in the third row are the “measured”  $S_0$  ( $\text{SNR} = \sqrt{1000}$ ), and the estimated unpolarized and polarized components of the scene after 200 iterations of LeMaster and Cain’s algorithm

Figure 2.4 depicts estimation results using simulated polarimetric imagery collected using three polarimetric channels. The analyzers in the three channels are oriented at  $0^\circ, 60^\circ$ , and  $120^\circ$ . The target scene has two objects—one fully polarized and the other unpolarized, as shown in the first row of Fig. 2.4. These objects are imaged through atmospheric turbulence whose short-exposure PSF ( $D/r_0 = 20$ ) is

shown in the second row. The third row contains the “measured”  $S_0$  with  $\text{SNR} = \sqrt{1000}$ . Also shown in the third row are the unpolarized and polarized components of the scene estimated after 200 iterations. Note that the object and its polarimetric content are fully recovered.

## 2.6 *Classifying the Material of an Unknown Object with DoLP Priors*

This section reviews a material classification method using degraded polarimetric imagery introduced by Hyde. Using a variant of the polarimetric ML blind-deconvolution algorithm developed by LeMaster and Cain, Hyde estimates the true object’s irradiance  $S_0$ , the DoLP, the AoP, and the PSF [11]. Unlike LeMaster and Cain, Hyde adds prior knowledge about the sought DoLP estimate, called the DoLP prior, into his algorithm to serve as a means to classify the unknown object. This DoLP prior distribution is simply referred to as the prior hereafter. Hyde introduces two priors—one representing dielectric materials and the other representing metallic materials. These priors are discussed in more detail in the next section. It should be noted that by introducing prior information about the sought parameters into the log-likelihood function, the problem changes from being an ML estimation problem to a maximum *a posteriori* (MAP) problem. Since MAP estimation is very similar in nature to ML estimation (previously reviewed), MAP estimation is not reviewed here. The interested reader is referred to Refs. [25] and [3] for more information.

*2.6.1 DOLP Priors.* Hyde adds two DoLP priors into his algorithm to classify dielectric and metallic materials [11,12]. To formulate these priors, he predicts the DoLPs of dielectrics and metals using a polarimetric bidirectional reflectance distribution function (pBRDF) [11]. These pBRDF results show that dielectric and metal DoLPs are uniformly distributed within certain nearly exclusive ranges [11]. He approximates the non-differentiable uniform distribution using a continuous super-Gaussian distribution as

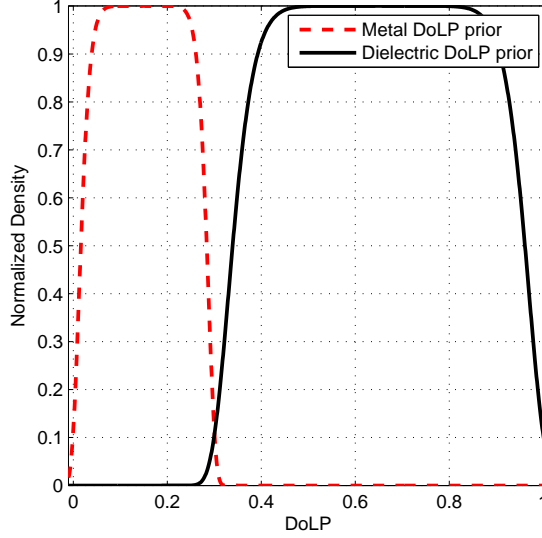


Figure 2.5: DoLP priors modeled with a super-Gaussian distribution. The constants in Eq. (2.54) are  $c = 1, \alpha = 7.2, \beta = 0.15, m = 10$  for the metal DoLP prior and  $c = 1, \alpha = 3.1, \beta = 0.65, m = 10$  for the dielectric DoLP prior [11].

$$\Pi(P) = c \exp \{ -[\alpha(P - \beta)]^m \}, \quad (2.54)$$

where  $P$  denotes the DoLP,  $c$  is a normalizing constant to ensure that  $\Pi(P)$  integrates to one,  $\alpha$  is a constant equivalent to the variance for the super-Gaussian distribution,  $\beta$  is a constant which controls the center of the distribution, and  $m$  is an even integer [11]. Figure 2.5 depicts the DoLP priors used by Hyde in [11].

The new complete-data log-likelihood function incorporating the DoLP prior is

$$\begin{aligned} L(P, S_0, \alpha, h) = & \sum_c \sum_{\mathbf{y}} \sum_{\mathbf{x}} \left\{ \tilde{d}_{uc}(\mathbf{y}, \mathbf{x}) \ln \left[ \frac{1}{2}(1 - P)S_0 h_c(\mathbf{y} - \mathbf{x}) \right] \right. \\ & \left. - \frac{1}{2}(1 - P)S_0 h_c(\mathbf{y} - \mathbf{x}) \right\} + \sum_c \sum_{\mathbf{y}} \sum_{\mathbf{x}} \left\{ \tilde{d}_{pc}(\mathbf{y}, \mathbf{x}) \ln [PS_0 \cos^2(\alpha(\mathbf{x}) - \theta_c) \right. \\ & \left. \times h_c(\mathbf{y} - \mathbf{x})] - PS_0 \cos^2(\alpha(\mathbf{x}) - \theta_c) h_c(\mathbf{y} - \mathbf{x}) \right\} + \sum_c \sum_{\mathbf{y}} \sum_{\mathbf{x}} \ln [\Pi(P)] \end{aligned} \quad (2.55)$$

where  $\tilde{d}_{uc}(\mathbf{y}, \mathbf{x})$  and  $\tilde{d}_{pc}(\mathbf{y}, \mathbf{x})$  are the incomplete data as defined in Eq. (2.47) [11]. In Hyde's algorithm, the AoP  $\alpha(\mathbf{x})$  is assumed to be zero, which implies that observation is made in the specular plane [11].

As in Schulz's and LeMaster and Cain's algorithms, Hyde employs the EM algorithm to find estimates of the desired parameters  $P, S_0, \alpha$ , and  $h_c$ . The outcome of the expectation step is the objective function  $Q$  which is [11]:

$$\begin{aligned}
Q^{n+1}(P, S_0, \alpha, h) = & \sum_c \sum_{\mathbf{y}} \sum_{\mathbf{x}} \left\{ E \left[ \tilde{d}_{uc}(\mathbf{y}, \mathbf{x}) \right] \ln \left[ \frac{1}{2} (1 - P^n) S_0^n h_c^n(\mathbf{y} - \mathbf{x}) \right] \right. \\
& \left. - \frac{1}{2} (1 - P^n) S_0^n h_c^n(\mathbf{y} - \mathbf{x}) \right\} + \sum_c \sum_{\mathbf{y}} \sum_{\mathbf{x}} \left\{ E \left[ \tilde{d}_{pc}(\mathbf{y}, \mathbf{x}) \right] \ln \left[ P^n S_0^n \cos^2(\alpha^n(\mathbf{x}) - \theta_c) \right] \right. \\
& \left. \times h_c^n(\mathbf{y} - \mathbf{x}) \right\} - P^n S_0^n \cos^2(\alpha^n(\mathbf{x}) - \theta_c) h_c^n(\mathbf{y} - \mathbf{x}) \left\} + \sum_c \sum_{\mathbf{y}} \sum_{\mathbf{x}} \ln [\Pi(P^n)]
\end{aligned} \tag{2.56}$$

Differentiating  $Q$  with respect to  $P, S_0, \alpha$ , and  $h_c$  and setting the derivatives equal to zero yield the update equations

$$\begin{aligned}
0 = & P(1 - P) \sum_c \sum_{\mathbf{y}} \frac{1}{\Pi(P)} \frac{d\Pi(P)}{dP} \\
& - P \sum_c \sum_{\mathbf{y}} (\psi_{uc}^{n+1}(\mathbf{y}, \mathbf{x}) + \psi_{pc}^{n+1}(\mathbf{y}, \mathbf{x})) + \sum_c \sum_{\mathbf{y}} \psi_{pc}^{n+1}(\mathbf{y}, \mathbf{x}) \\
S_0 = & \frac{2}{C} \sum_c \sum_{\mathbf{y}} (\psi_{uc}^{n+1}(\mathbf{y}, \mathbf{x}) + \psi_{pc}^{n+1}(\mathbf{y}, \mathbf{x})) \\
0 = & \sum_c \sum_{\mathbf{y}} \psi_{pc}^{n+1} \tan(\alpha(\mathbf{x}) - \theta_c) \\
h_c(\mathbf{z}) = & \frac{1}{D_c} \sum_{\mathbf{y}} [\psi_{uc}^{n+1}(\mathbf{y}, \mathbf{y} - \mathbf{z}) + \psi_{pc}^{n+1}(\mathbf{y}, \mathbf{y} - \mathbf{z})]
\end{aligned} \tag{2.57}$$

where

$$\begin{aligned}\psi_{uc}^{n+1}(\mathbf{y}, \mathbf{x}) &= E \left[ \tilde{d}_{uc}(\mathbf{y}, \mathbf{x}) | d_c, P^n, S_0^n, \alpha^n, h_c^n \right] = \frac{1}{2} \frac{d_c}{i_c^n} (1 - P^n) S_0^n h_c^n \\ \psi_{pc}^{n+1}(\mathbf{y}, \mathbf{x}) &= E \left[ \tilde{d}_{pc}(\mathbf{y}, \mathbf{x}) | d_c, P^n, S_0^n, \alpha^n, h_c^n \right] = \frac{d_c}{i_c^n} P^n S_0^n \cos^2(\alpha^n - \theta_c) h_c^n\end{aligned}, \quad (2.58)$$

$\mathbf{z} = \mathbf{y} - \mathbf{x}$ , and  $D_c = \sum_y d_c(\mathbf{y})$  [11]. The channel PSF  $h_c(\mathbf{z})$  is estimated according to Schulz's parameterized PSF technique introduced in Section 2.4. Applying the DoLP prior model  $\Pi(P)$  in Eq. (2.54) to the DoLP update equation in the first row of Eq. (2.57) yields a DoLP update equation of the form [11]

$$\begin{aligned}0 &= m\alpha^m P^2 (P - \beta)^{m-1} - m\alpha^m P (P - \beta)^{m-1} \\ &- P \sum_c \sum_y [\psi_{uc}^{n+1}(\mathbf{y}, \mathbf{x}) + \psi_{pc}^{n+1}(\mathbf{y}, \mathbf{x})] + \sum_c \sum_y \psi_{pc}^{n+1}(\mathbf{y}, \mathbf{x})\end{aligned}. \quad (2.59)$$

To classify each pixel, two sets of estimates for the parameters  $P, S_0$ , and  $h$  are computed from Eq. (2.57), given the metal and dielectric priors [11]. These two sets of estimates are then substituted into the objective function  $Q$  which is simplified in Eq. (3.1) using Eqs. (2.56) and (2.58). Whichever set of estimates maximizes  $Q$  classifies that pixel either as a metal or as a dielectric.

Figure 2.6 depicts the recovery of the target scene from turbulence-degraded ( $D/r_0 = 20$ ) images using four polarimetric channels, i.e.,  $\theta = 0^\circ, 45^\circ, 90^\circ, 135^\circ$ . The first row of the figure is the true target scene, which consists of an object composed of metallic and dielectric components. The portions of the object with the lower DoLP  $P = 0.2$  represent metallic components; the portions with the higher DoLP  $P = 0.7$  represents dielectric components. The “measured”  $S_0$  ( $\text{SNR} = \sqrt{1000}$ ) and DoLP are shown in the second row. The third row contains the estimates of the scene, applying the update equations in Eq. (2.57), after 200 iterations. Figure 2.7 shows the material classification results, incorporating Hyde's metal and dielectric DoLP priors. As Figs. 2.6 and 2.7 indicate, the algorithm successfully recovers and classifies the target scene.



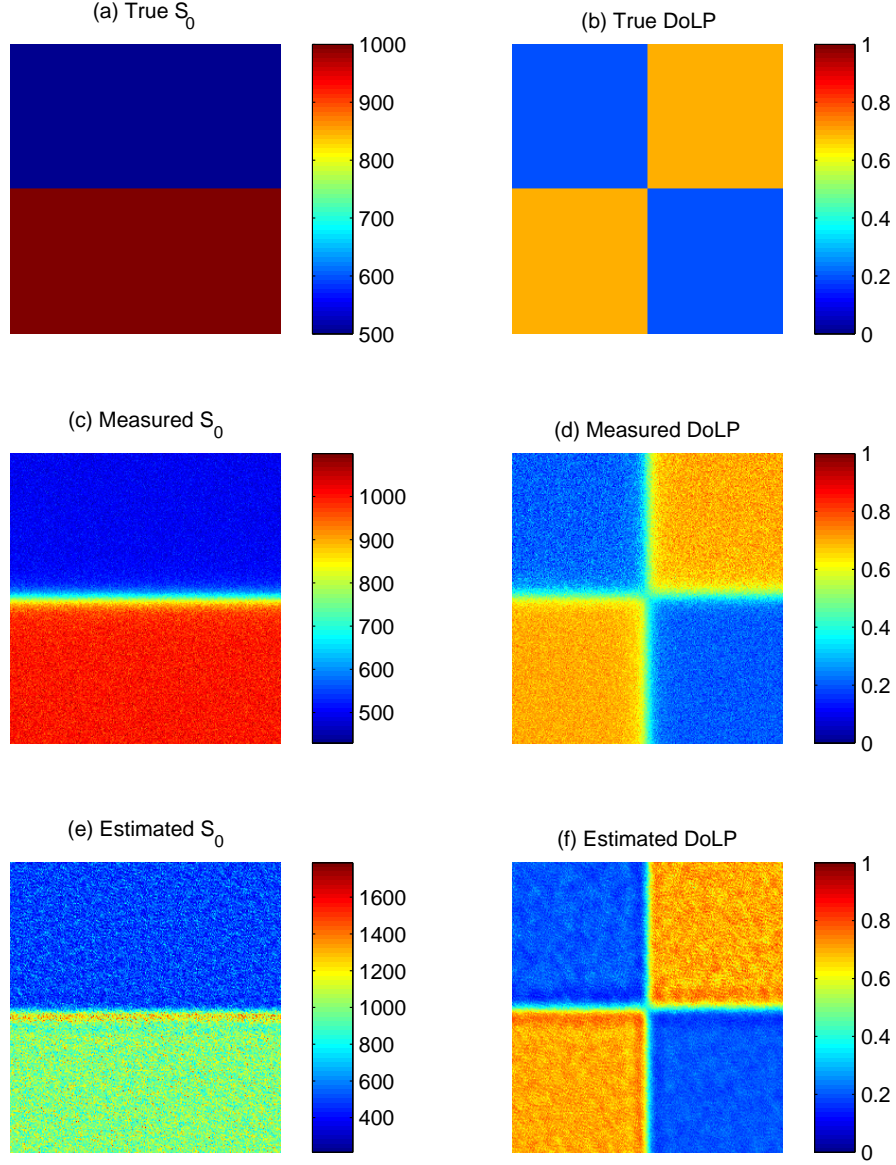


Figure 2.6: Estimation results using four-channel ( $0^\circ, 45^\circ, 90^\circ, 135^\circ$ ) polarimetric imagery. The top row is the true target scene. The second row shows measurements ( $\text{SNR} = \sqrt{1000}$ ) degraded by atmospheric turbulence ( $D/r_0 = 20$ ). The third row contains the final estimation results after 200 iterations.

*2.6.2 Limitations.* In Hyde's algorithm, fixed DoLP priors are used to classify the unknown object. A key limitation of this approach lies in the fact that natural materials weakly polarize scattered light at near-normal incident angles [11]. As a result, the images collected at near-normal geometries ( $\theta_i, \theta_r = 24^\circ$  in Hyde's paper) are poorly classified by his material-classification algorithm [11]. Hyde suggests that this

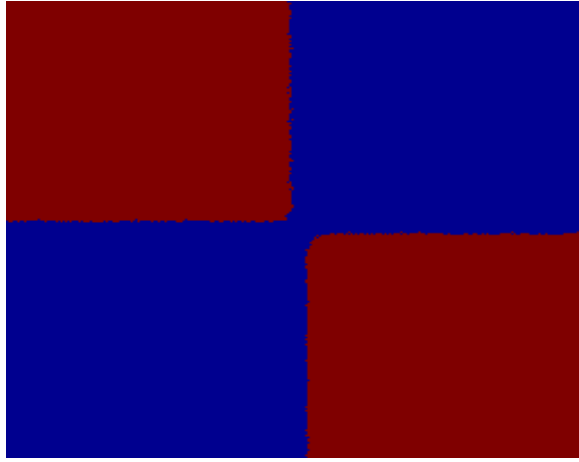


Figure 2.7: Binary material classification of an unknown object (red = metal, blue = dielectric).

limitation can be alleviated by adaptively updating the DoLP priors as more information becomes available about the scene [11]. Chapter III presents a methodology to implement the adaptive DoLP priors suggested by Hyde and represents the main theoretical thrust of this research.

### III. Research Methodology

This chapter describes a methodology to implement a polarization-based material-classification algorithm incorporating adaptive DoLP priors. The process involves updating the DoLP priors by inspecting the distribution of DoLP estimates to enhance classification results at near-normal collection geometries.

#### 3.1 Material Classification

The material-classification algorithm introduced by Hyde classifies the materials of an unknown object using polarimetric imagery degraded by the atmosphere. Incorporated in his algorithm are DoLP priors of a metal and a dielectric. The classification is made by comparing the values of the objective function  $Q$  of each DoLP estimate as described in Section 2.6.1.

Given the metal and dielectric DoLP priors, the first update equation in Eq. (2.57) produces two DoLP estimates  $P$ . To compute the value of  $Q$  for each material class, these DoLP estimates are substituted into Eq. (3.1), which is obtained from Eqs. (2.56) and (2.58), along with the estimates of the remaining parameters  $S_0$ ,  $h_c$ , and  $i_c$ :

$$\begin{aligned}
 Q^{n+1}(P, S_0, \alpha, h) = & [\chi_{\text{est,u}}^n \ln(\chi_{\text{prior,u}}^{n+1}) + \chi_{\text{est,p}}^n \ln(\chi_{\text{prior,p}}^{n+1})] \\
 \times \sum_c \sum_{\mathbf{y}} & \left[ \frac{d_c(\mathbf{y})}{i_c^n(\mathbf{y})} h_c^n(\mathbf{y} - \mathbf{x}_0) \right] + (\chi_{\text{est,u}}^n + \chi_{\text{est,p}}^n) \sum_c \sum_{\mathbf{y}} \left\{ \frac{d_c(\mathbf{y})}{i_c^n(\mathbf{y})} h_c^n(\mathbf{y} - \mathbf{x}_0) \right. \\
 & \times \ln[h_c^{n+1}(\mathbf{y} - \mathbf{x}_0)] \Big\} - C(\chi_{\text{est,u}}^n + \chi_{\text{est,p}}^n)
 \end{aligned} \quad (3.1)$$

where

$$\begin{aligned}
 \chi_{\text{est,u}}^n &= \frac{1}{2} [1 - P^n(\mathbf{x}_0)] S_0^n(\mathbf{x}_0) \\
 \chi_{\text{est,p}}^n &= P^n(\mathbf{x}_0) S_0^n(\mathbf{x}_0) \cos^2[\alpha^n(\mathbf{x}_0) - \theta_c] \\
 \chi_{\text{prior,u}}^{n+1} &= \frac{1}{2} [1 - P_{\text{prior}}^{n+1}(\mathbf{x}_0)] S_0^{n+1}(\mathbf{x}_0) \\
 \chi_{\text{prior,p}}^{n+1} &= P_{\text{prior}}^{n+1}(\mathbf{x}_0) S_0^{n+1}(\mathbf{x}_0) \cos^2[\alpha^{n+1}(\mathbf{x}_0) - \theta_c]
 \end{aligned} \quad (3.2)$$

In Eq. (3.2), the subscripts  $n$  and  $n + 1$  indicate estimates at the  $n^{\text{th}}$  (previous) and  $(n + 1)^{\text{th}}$  (current) iterations,  $P^n(\mathbf{x}_0)$  is the previous DoLP estimate at pixel  $\mathbf{x}_0$ ,  $P_{\text{prior}}^{n+1}(\mathbf{x}_0)$  is the current DoLP estimate at  $\mathbf{x}_0$  computed using the metal or dielectric DoLP prior, and  $C$  is the total number of polarization channels. The DoLP estimate (either the estimate using the metal DoLP prior or the estimate using the dielectric DoLP prior) which maximizes  $Q$  determines whether the material is classified as a metal or a dielectric at pixel  $\mathbf{x}_0$ :

$$\text{material at } \mathbf{x}_0 = \begin{cases} \text{metal} & Q_d(\mathbf{x}_0) - Q_m(\mathbf{x}_0) \leq 0 \\ \text{dielectric} & \text{else} \end{cases} \quad (3.3)$$

where  $Q_d(\mathbf{x}_0)$  and  $Q_m(\mathbf{x}_0)$  denote the  $Q$  values using the dielectric and the metal DoLP priors at pixel  $\mathbf{x}_0$ , respectively [11].

### 3.2 Adaptive DoLP Priors

Section 2.6.2 mentions that natural materials weakly polarize scattered light at near-normal incident angles. This causes Hyde’s material-classification algorithm to perform poorly at near-normal collection geometries [11]. Figure 3.1 depicts the probability distributions of the measured DoLP at incident angles  $\theta_i = 50^\circ$  and  $\theta_i = 24^\circ$ . The target scene consists of metal and dielectric parts. The probability distribution at  $\theta_i = 50^\circ$  is consistent with Hyde’s DoLP priors shown in Fig. 2.5. Contrast this with the distribution shown in Fig. 3.1(b). The range of DoLP values observed in the  $\theta_i = 24^\circ$  case is approximately 1/4 of the  $\theta_i = 50^\circ$  case, which demonstrates the main limitation of Hyde’s implementation. The threshold between the metal and dielectric DoLP values at the  $\theta_i = 24^\circ$  geometry becomes so low that Hyde’s fixed DoLP prior models are not able to accurately classify materials in this scenario. Hyde suggests that this limitation can be alleviated by adaptively updating the DoLP priors as more information about the scene becomes available [11]. The following sections introduce three novel approaches to implement adaptive DoLP priors, termed hereafter higher-order super-Gaussian method, Gaussian method, and distribution-averaging method.

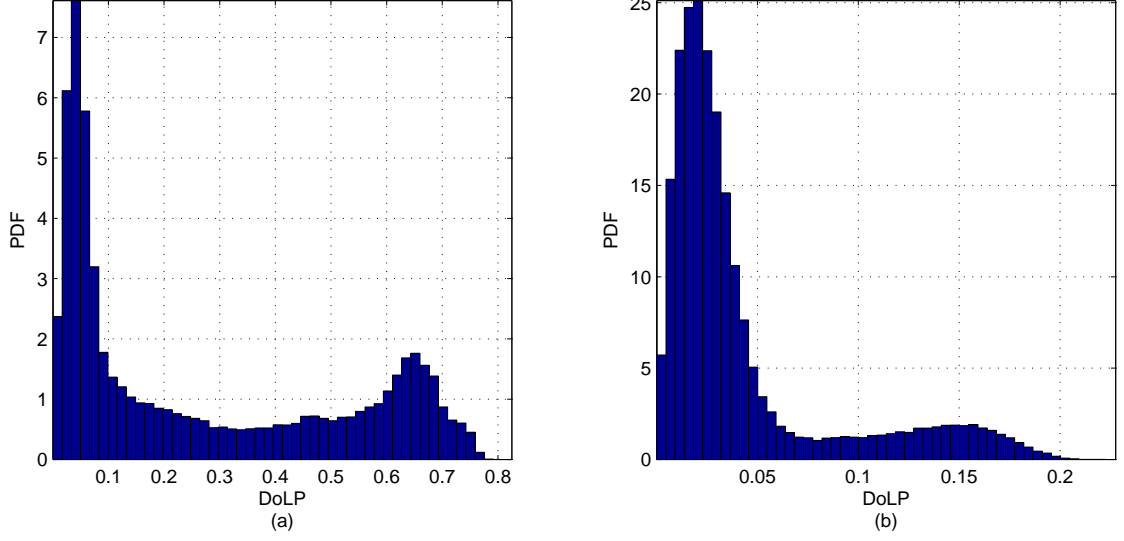


Figure 3.1: (a) Distribution of measured DoLP at  $\theta_i = 50^\circ$ . (b) Distribution of measured DoLP at  $\theta_i = 24^\circ$ .

*3.2.1 Higher-Order Super-Gaussian Method.* Hyde’s pBRDF study finds that the DoLP is best modeled as a uniform probability density between 0 and 1 because of numerous uncontrollable factors such as observation geometry and surface state [11]. In order to derive the DoLP update equations in Eq. (2.59), the uniform distribution of the DoLP prior needs to be modeled with a differentiable distribution for which a continuous super-Gaussian distribution in Eq. (2.54) is chosen [11].

In the higher-order super-Gaussian method, the sum of two super-Gaussian distributions is fit to the estimated DoLP distribution. The fit function is of the form

$$\Pi(P) = c_m e^{-[a_m(P-b_m)]^m} + c_d e^{-[a_d(P-b_d)]^m}, \quad (3.4)$$

where the coefficients  $c_m$  and  $c_d$  are normalizing factors,  $a_m$  and  $a_d$  determine the widths of the super-Gaussians,  $b_m$  and  $b_d$  determine the centers of the super-Gaussians, and  $m$  is the order [11, 13]. The subscripts  $m$  and  $d$  represent a metal and a dielectric, respectively. Figure 3.2(a) shows the resulting fit of Eq. (3.4) with the estimated DoLP distribution at  $\theta_i = 24^\circ$ . Figure 3.2(b) shows the resulting adaptive DoLP

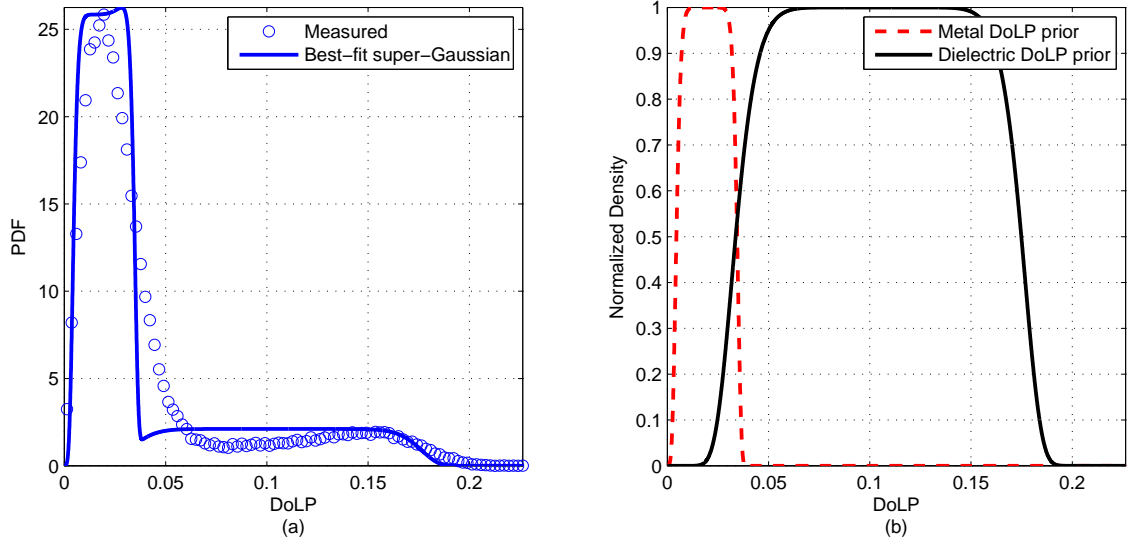


Figure 3.2: Higher-order super-Gaussian method for adaptive DoLP priors. (a) Distribution of DoLP measurements and the fit of Eq. (3.4) when  $m = 10$ . (b) Metal and dielectric priors formed from fit. The constants in Eq. (3.4) determined by the fit are  $c_m = 1$ ,  $a_m = 64.3$ ,  $b_m = 0.0195$  and  $c_d = 1$ ,  $a_d = 13.7$ ,  $b_d = 0.104$ .

priors obtained from the fit shown in Fig. 3.2(a). The obtained coefficients are then substituted into the update equation in Eq. (2.59) to compute the metal and dielectric DoLP estimates. The pixel is then classified using Eq. (3.3).

This approach is analytically sound, but has a major drawback. Figure 3.2 reveals that the higher-order super-Gaussian fitting and the prior-formation processes generate a threshold which is significantly lower than the one empirically observed in the DoLP distribution. As will be shown, this drawback leads to significant classification errors.

**3.2.2 Gaussian method.** Equation (2.15) states that the DoLP is the ratio of the linearly polarized irradiance to the total irradiance. Thus, assuming that shot noise is the dominant noise source, DoLP measurements observed at a given collection geometry and surface state should follow the random variable distribution formed by dividing two Poisson random variables. Unfortunately, no analytical form exists for this PDF. Figure 3.3 shows a PDF of this distribution obtained via Monte Carlo

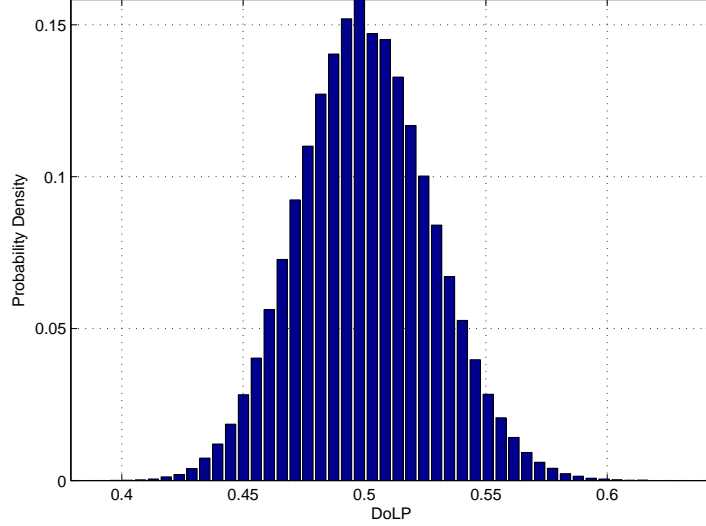


Figure 3.3: PDF of the division of two Poisson random variables using Monte Carlo analysis. The plot shows the PDF of DoLP measurements of a target whose true DoLP is 0.5 ( $\text{SNR} = \sqrt{1000}$ ).

analysis. The figure shows the distribution of DoLP measurements of a target whose true DoLP is 0.5 ( $\text{SNR} = \sqrt{1000}$ ). Note that the DoLP PDF is very Gaussian-like. Based on this finding, it seems much more reasonable to fit the sum of two Gaussian functions to the estimated DoLP distribution than it does super-Gaussians. Thus, in the Gaussian method,

$$\Pi(P) = c_m e^{-[a_m(P-b_m)]^2} + c_d e^{-[a_d(P-b_d)]^2} \quad (3.5)$$

is fit to the measured DoLP PDF.

Fig. 3.4(a) shows the result of this fit for DoLP measurements at  $\theta_i = 24^\circ$ . The figure shows that the Gaussian fit models DoLP measurements more accurately than super-Gaussian fit depicted in Fig. 3.2(a). This Gaussian fit provides the threshold between a metal and a dielectric from which the DoLP priors can be built. As mentioned in the previous section, the super-Gaussian distribution is chosen to model the uniform distribution of the overall DoLP. In order to compute the coefficients in Eq. (3.4) necessary to model the updated DoLP priors using the super-Gaussian distribution, the threshold between the two materials are determined by finding the

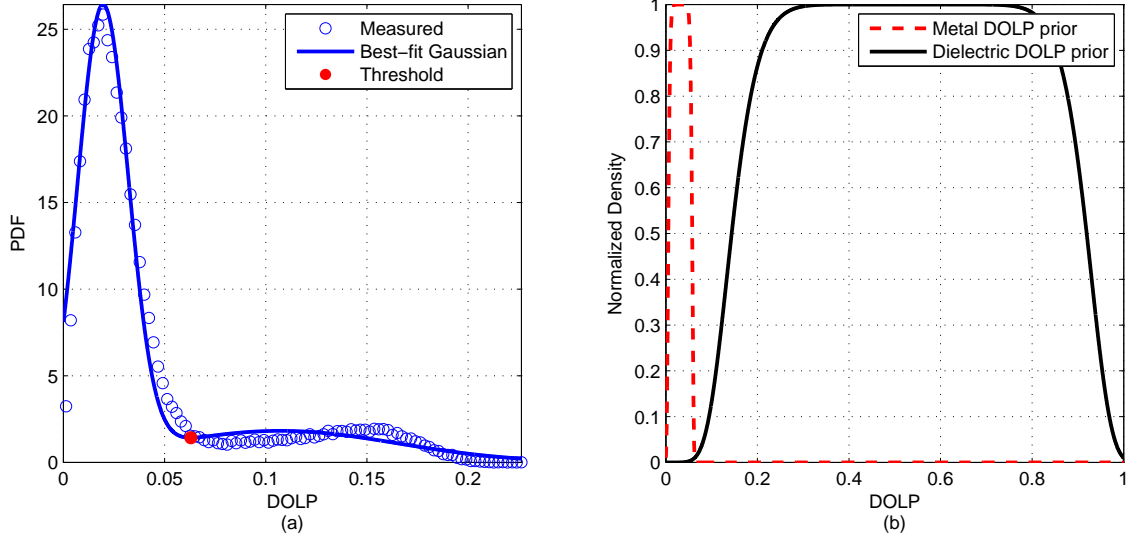


Figure 3.4: Gaussian method for adaptive DoLP priors. (a) Distribution of DoLP measurements and the fit of Eq. (3.5). (b) Metal and dielectric priors formed from fit. The constants in Eq. (3.5) determined by the fit are  $c_m = 1$ ,  $a_m = 34.5$ ,  $b_m = 0.0315$  and  $c_d = 1$ ,  $a_d = 2.32$ ,  $b_d = 0.532$ .

minimum between the two maxima of the Gaussian fit (marked in Fig. 3.4(a)). The center of each prior is then obtained by computing the midpoint between the threshold and the DoLP values of 0 and 1. Given the threshold and the center of a prior, the coefficient  $a$  is computed using Eq. (2.54), i.e.,

$$a = \frac{[-\ln \Pi(P_{th})]^{1/m}}{(P_{th} - b)} \quad (3.6)$$

where  $P_{th}$  is the DoLP value at the threshold and  $\Pi(P_{th})$  is a user-chosen quantity. In this analysis, its value is chosen to be 0.01. Figure 3.4(b) shows the updated DoLP priors with the coefficients computed as described.

*3.2.3 Distribution-Averaging Method.* The final method investigated for adaptively updating the DoLP priors is to approximate the threshold by finding the mean of the measured DoLP distribution. It has been found empirically that the mean of the distribution lies approximately at the intersection (or threshold) of the



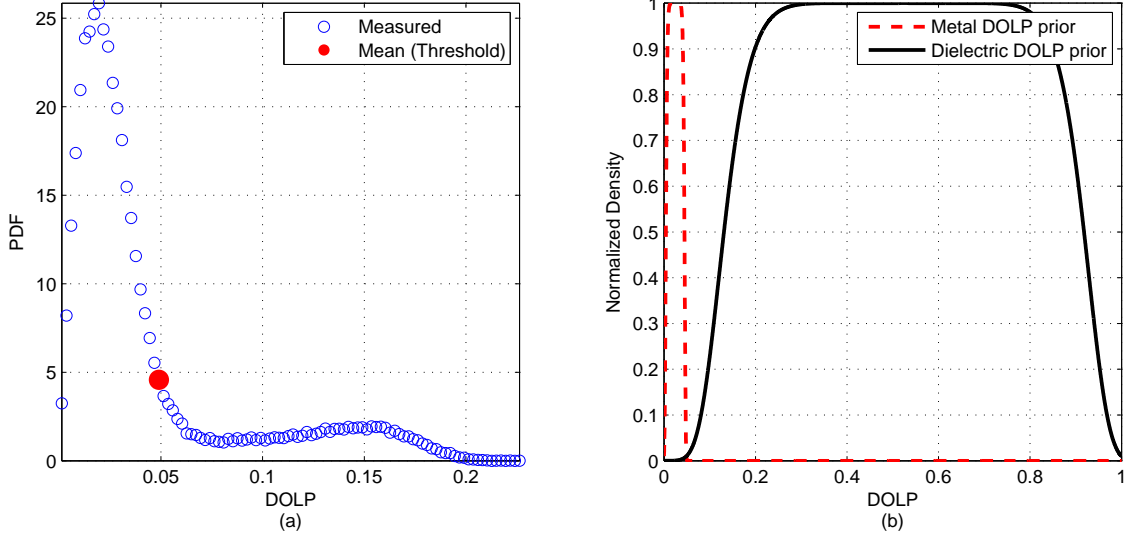


Figure 3.5: Distribution-averaging method for adaptive DoLP priors. (a) Distribution of DoLP measurements and the calculated mean. (b) Updated DoLP priors. The constants in Eq. (3.4) determined by the mean are  $c_m = 1$ ,  $a_m = 45.4$ ,  $b_m = 0.0257$  and  $c_d = 1$ ,  $a_d = 2.46$ ,  $b_d = 0.109$ .

two “humps” of the DoLP distribution. In order to update the DoLP priors, the coefficients of the super-Gaussian distribution in Eq. (3.4) are computed from the threshold and the DoLP values of 0 and 1, using the same process as in the Gaussian method. Figure 3.5(b) shows the resulting metal and dielectric DoLP priors.

### 3.3 Algorithm Execution

Figure 3.6 outlines a flow of the proposed material-classification algorithm at the  $i^{\text{th}}$  iteration. The number of iterations before forming the priors and classifying the object is determined by comparing the DoLP estimates (obtained using standard LeMaster and Cain deconvolution) to the DoLP obtained from turbulence-free polarimetric images. The root mean squared error (RMSE) of DoLP estimates in Fig. 3.7(a) indicates that the DoLP estimate is optimized at about 50 iterations. Thus, on the 51<sup>st</sup> iteration, the DoLP priors are updated using one of three techniques developed in this chapter and the binary classification of the objects in the scene commences.

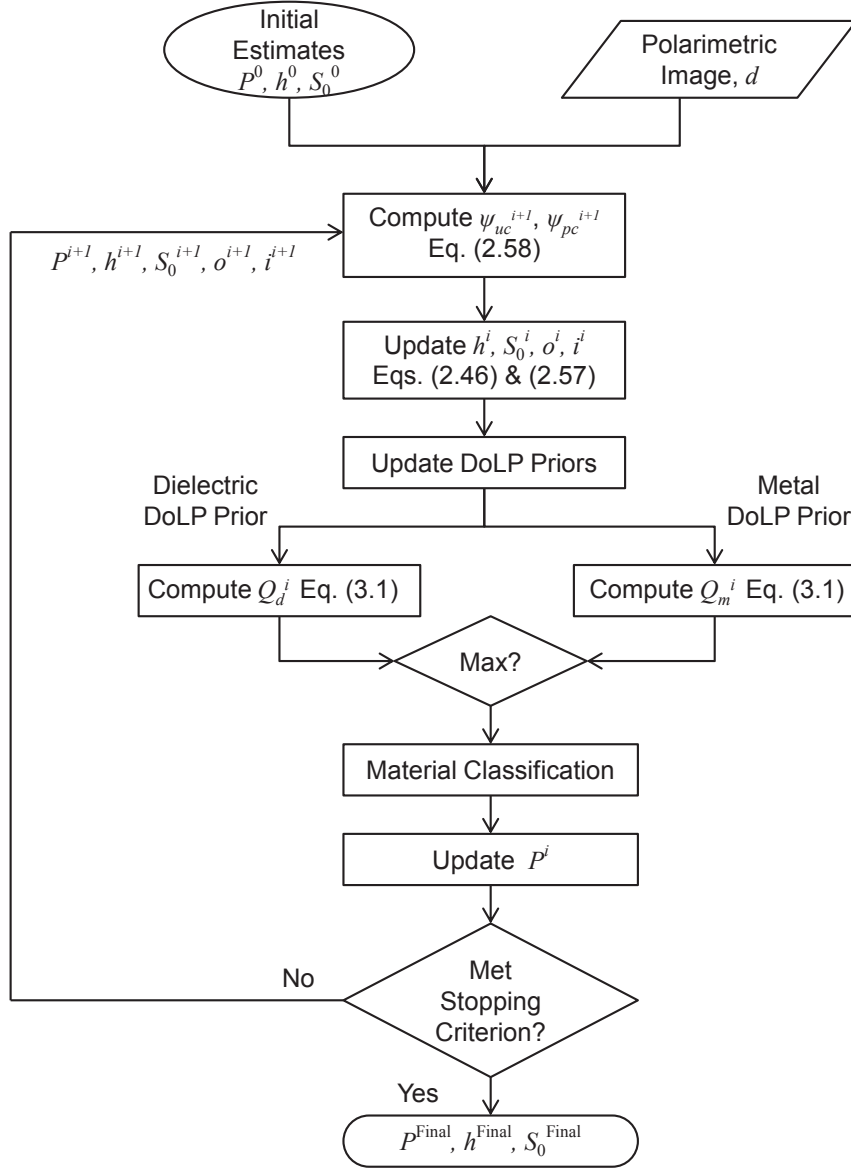


Figure 3.6: Flowchart of the proposed material-classification algorithm augmented with adaptive DoLP priors at the  $i^{\text{th}}$  iteration.

The stopping criterion for the algorithm is decided based on the  $S_0$  estimation results. Shown in Fig. 3.7(b) is the RMSE of the  $S_0$  estimation where the irradiance of the object measured without atmospheric turbulence is considered the true object irradiance. Note that the turbulence-free images do contain static aberrations due to the imperfect imaging system. This explains why the  $S_0$  RMSE increases with

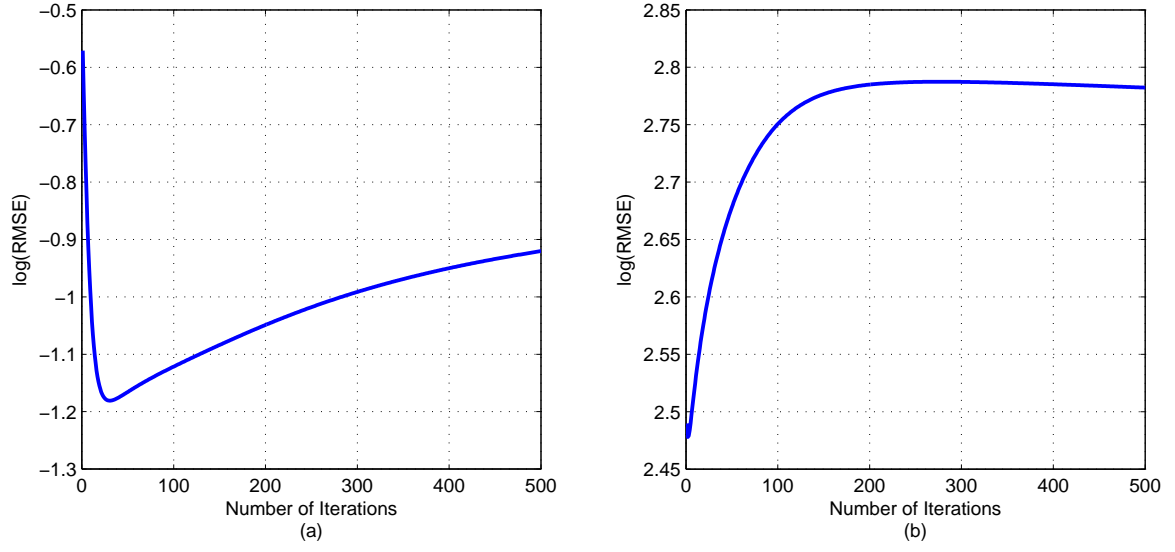


Figure 3.7: (a) RMSE of DoLP to determine the iteration number to update DoLP priors. (b) RMSE of  $S_0$  to determine the stopping criterion for the material-classification algorithm.

the number of iterations before converging. Based on the observation that the  $S_0$  estimation stagnates after 300 iterations, the entire algorithm is stopped after 300 iterations.

## IV. Results and Analysis

This chapter presents results of the material-classification algorithm introduced in Chapter 3. Section 4.1 describes the experimental design and procedures. Sections 4.2 and 4.3 discuss classification results of the algorithm using fixed and adaptive DoLP priors. A spatial error analysis of the results is also presented in Section 4.4.

### 4.1 Experimental Setup

The images analyzed in this research were collected by Hyde using a Stokes polarimeter in the Optical Turbulence Estimation, Compensation, and Simulation laboratory at the Air Force Institute of Technology. Figure 4.1 shows the instrument, which consists of three main sections. The source/sample section consists of two optical rotation stages. The lower rotation stage holds the sample while the upper rotation stage, which is placed on the top of the lower rotation stage, holds the 1550 nm light emitting diode source. These two stages are rotated in combination to yield any  $\theta_i + \theta_r \geq 48^\circ$  where  $\theta_i$  and  $\theta_r$  denote the incident and reflected angles, respectively. Aluminum and steel samples are partially painted to simulate a target scene

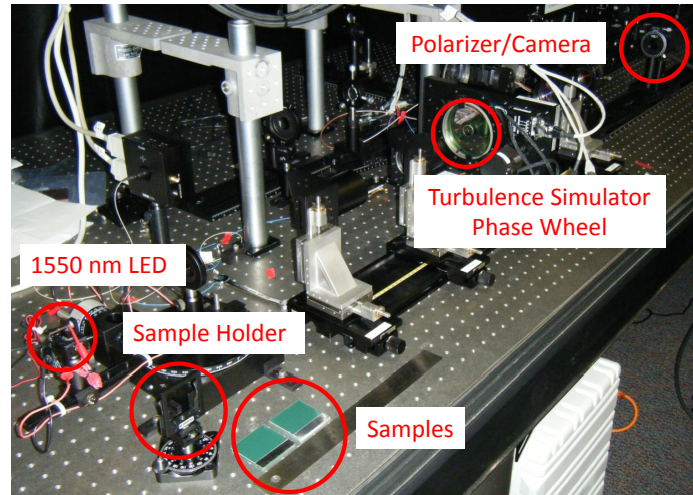


Figure 4.1: Photograph of the Stokes polarimeter used to collect the polarimetric imagery in this experiment [11].

consisting of metal and dielectric parts. The atmospheric turbulence simulator section of the instrument models various atmospheric turbulence conditions by changing the location of a phase wheel. Atmospheric turbulence conditions used in this research are  $D/r_0 \approx 7.9, 10.5$ , and  $12.9$ . The last section of the instrument is the polarimetric imager which includes an imaging lens (pupil size of  $25\text{ mm}$ ), a rotating linear polarizer, and a digital camera whose array size is  $250 \times 316$  with a pixel pitch of  $30\text{ }\mu\text{m}$ . For more details about the experimental setup, the reader is referred to [11].

In order to implement the proposed material-classification algorithm, the Stokes parameters  $S_0$ ,  $S_1$ , and  $S_2$  are extracted from four polarimetric images ( $\theta_c = 0^\circ, 45^\circ, 90^\circ, 135^\circ$ ). Dark-frame images were collected and subtracted from the polarimetric images before computing the Stokes parameters. The original images of size  $250 \times 316$  are padded to size  $512 \times 512$  and then spatially windowed using a Tukey window to prevent “ringing” caused by the fast Fourier transforms used in the algorithm.

The algorithm starts with choosing initial estimates of the sought parameters— $P$ ,  $S_0$ , and the PSF  $h_c$ . The initial estimates of  $P$  and  $S_0$  are  $512 \times 512$  arrays of  $1/2$  and  $1$ , respectively. The initial estimate of  $h_c$  is formed from a randomly drawn atmospheric phase screen ( $D/r_0 = 10$ ) with piston and tilt removed.

## 4.2 Classification Results—Fixed DoLP Priors

Figure 4.2 shows results of the material-classification algorithm with Hyde’s DoLP priors for the painted aluminum target after 300 iterations. The atmospheric turbulence condition and the collection geometry are  $D/r_0 \approx 7.9$  and  $\theta_i = \theta_r = 50^\circ$ , respectively. Figures 4.2(a), (d), and (g) show  $S_0$  images of no-turbulence, turbulence-degraded, and estimated data, respectively. The experimental  $P$  results are shown in Figs. 4.2(b), (e), and (h). The threshold of  $P = 0.3$  is chosen to discriminate between a metal ( $P < 0.3$ ) and a dielectric ( $P \geq 0.3$ ) for the no-turbulence and turbulence-degraded results. This threshold value is the intersection of the two DoLP priors as shown in Fig. 2.5. The corresponding material-classification results are shown in Figs. 4.2(c), (f), and (i). As indicated by Hyde’s previous research, the estimated classifi-

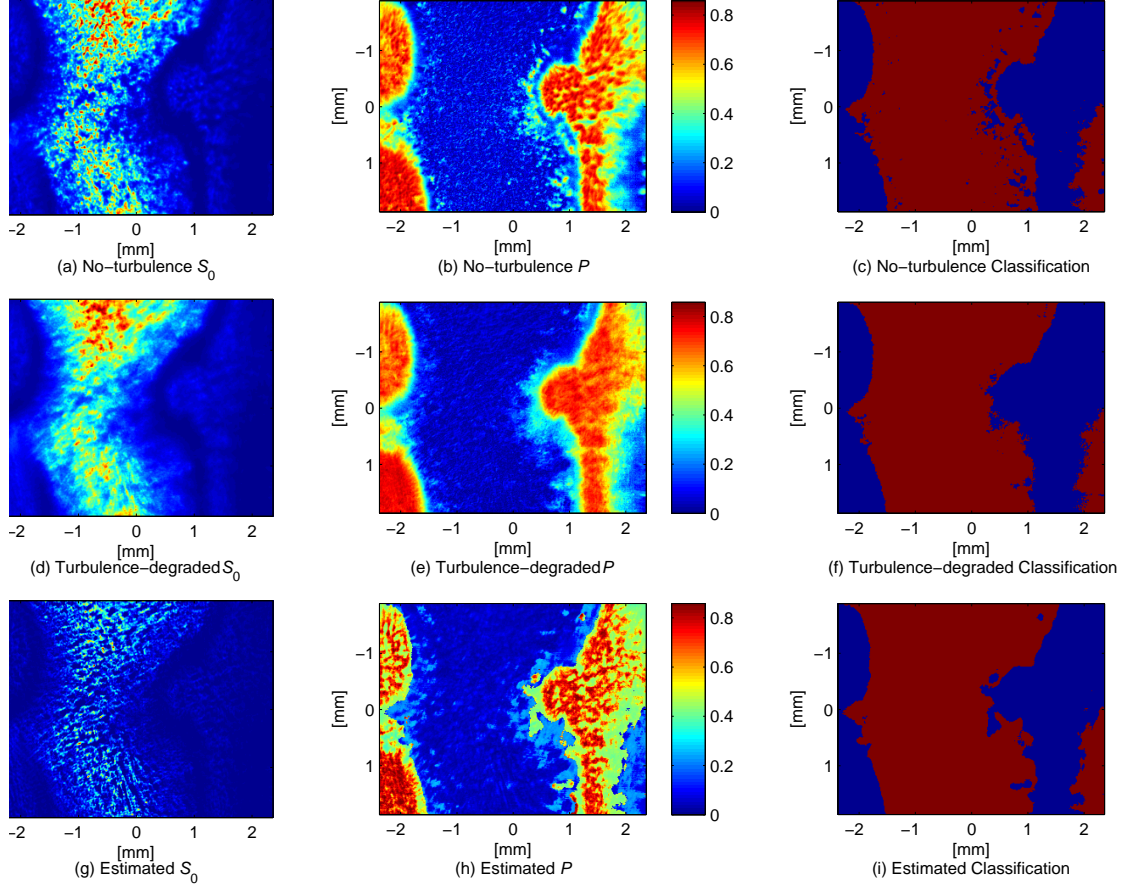


Figure 4.2: Results of Hyde’s material-classification algorithm for the painted aluminum target ( $D/r_0 \approx 7.9$  and  $\theta_i = \theta_r = 50^\circ$ ). For the no-turbulence and the turbulence-degraded measurements,  $P \geq 0.3$  is classified as a dielectric and  $P < 0.3$  as a metal. The estimated classification result is based on the metal and dielectric DoLP priors developed by Hyde and reviewed in Section 2.6.1. In the classification results, the blue color implies dielectric and the red color implies metal. The final estimates are obtained after 300 iterations.

cation result in Fig. 4.2(i) reveals that the algorithm not only accurately classifies the object but also recovers details of the target scene lost by atmospheric turbulence, evident in the estimated  $P$  result.

Figure 4.3, on the other hand, illustrates the limitation of the algorithm using fixed DoLP priors for near-normal collection geometries ( $\theta_i = \theta_r = 24^\circ$  in this case). The threshold of  $P = 0.08$  is chosen from the histogram of the DoLP measurements in Fig. 3.1(b) to discriminate between a metal ( $P < 0.08$ ) and a dielectric ( $P \geq 0.08$ )

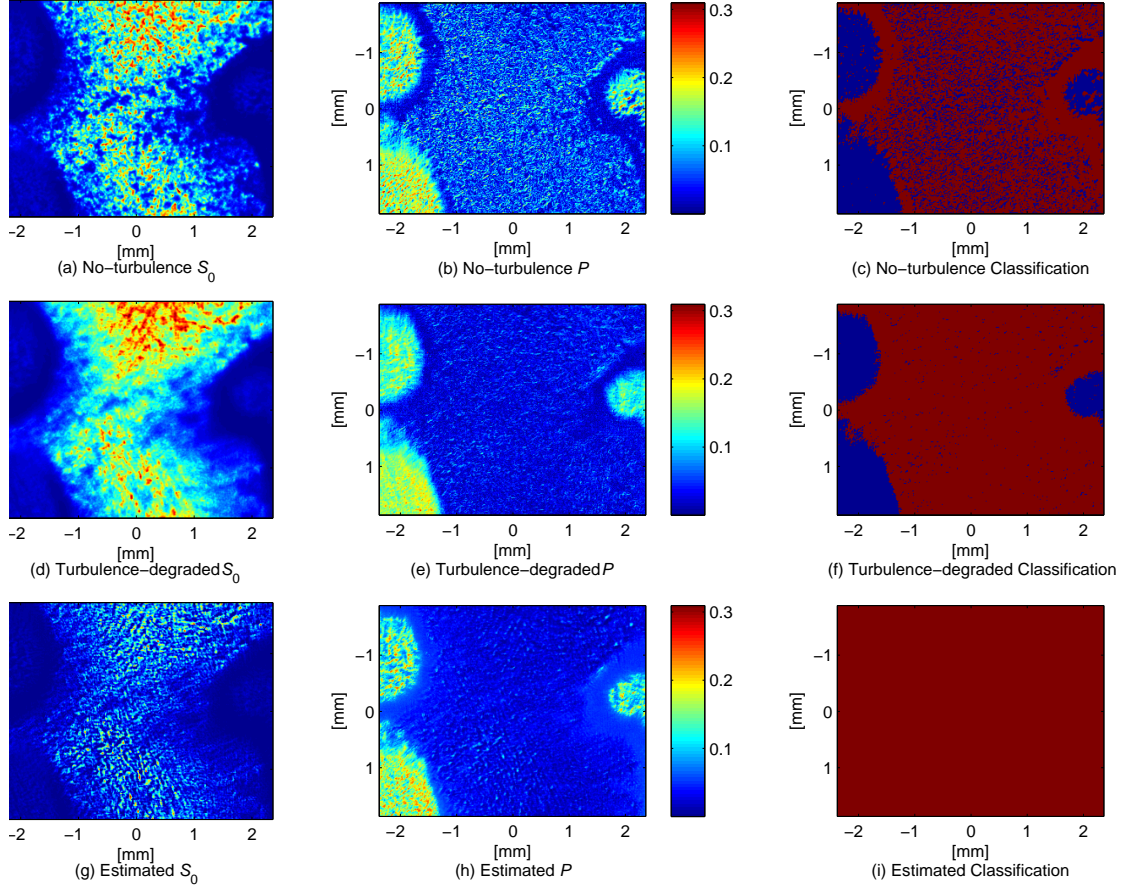


Figure 4.3: Results of Hyde's material-classification algorithm for the painted aluminum target ( $D/r_0 \approx 7.9$  and  $\theta_i = \theta_r = 24^\circ$ ). For the no-turbulence and the turbulence-degraded measurements,  $P \geq 0.08$  is classified as a dielectric and  $P < 0.08$  as a metal. The estimated classification result is based on the metal and dielectric DoLP priors developed by Hyde and reviewed in Section 2.6.1. In the classification results, the blue color implies dielectric and the red color implies metal. The final estimates are obtained after 300 iterations.

for the no-turbulence and turbulence-degraded data. To demonstrate the limitation of the algorithm in this near-normal geometry, the DoLP priors developed by Hyde and reviewed in Section 2.6.1 are incorporated into the algorithm for material classification. The estimated classification result in Fig. 4.3(i) confirms the predicted poor performance of the algorithm for near-normal collection geometries.

### 4.3 Classification Results—Adaptive DoLP Priors

In order to alleviate the near-normal collection geometry limitation of the fixed-prior material-classification algorithm, the DoLP priors should be updated as more information about the target scene becomes available. The following sections present classification results of the three DoLP prior update methods developed in Chapter III.

*4.3.1 Higher-Order Super-Gaussian Method.* Figure 4.4 shows results of the material-classification using adaptive DoLP priors updated by the higher-order super-Gaussian method discussed in Section 3.2.1. The same images of the painted aluminum target ( $D/r_0 \approx 7.9$ ,  $\theta_i = \theta_r = 24^\circ$ ) in Fig. 4.3 are used for the proposed method. In order to classify the no-turbulence and the turbulence-degraded measurements, the threshold value is computed by fitting the distribution of each DoLP measurement with the higher-order super-Gaussian function as described in Section 3.2.1. The resulting thresholds of  $P = 0.0618$  and  $P = 0.0464$  are then applied to classify the no-turbulence and the turbulence-degraded data, respectively.

The estimated classification result using the updated DoLP priors is shown in Fig. 4.4(i). Note that the figure depicts only a few pixels correctly classified as metal. Figure 4.4(i) indicates that the algorithm with DoLP priors updated by the higher-order super-Gaussian method performs as poorly as the algorithm with fixed DoLP priors shown in Fig. 4.3(i). As mentioned in Section 3.2.1, the higher-order super-Gaussian method yields a lower threshold than the one empirically observed in the measured DoLP distribution. This causes the incorrect dielectric over classification. Although the estimated classification result of the higher-order super-Gaussian method is poor, the blind-deconvolution algorithm still produces  $S_0$  and  $P$  estimates with recovered details lost in the turbulence-degraded images.

*4.3.2 Gaussian Method.* Figure 4.5 shows results of the material-classification algorithm using DoLP priors adaptively updated by the Gaussian method discussed in Section 3.2.2. The images of the target and the layout of the figure are identical to



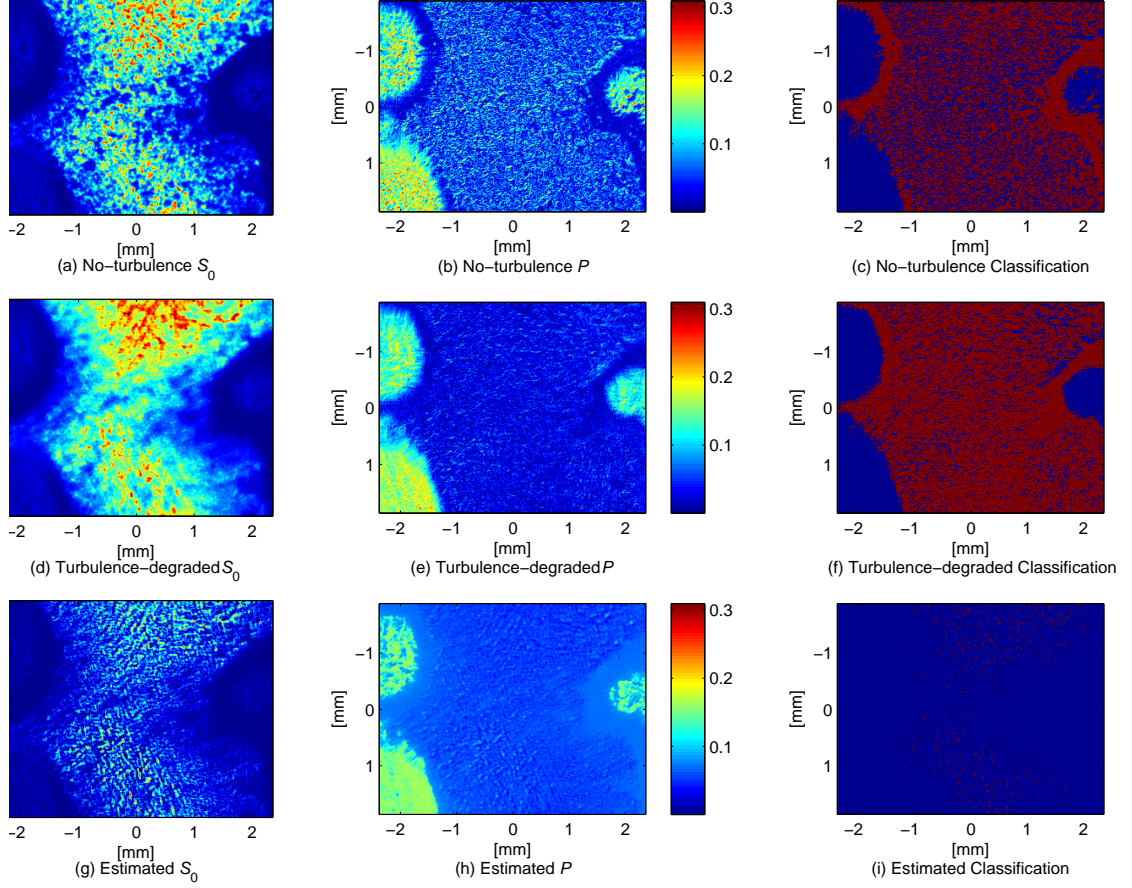


Figure 4.4: Results of the material-classification algorithm using adaptive DoLP priors derived from the higher-order super-Gaussian method for the painted aluminum target ( $\theta_i = \theta_r = 24^\circ$  and  $D/r_0 \approx 7.9$ ). The thresholds for classifying the no-turbulence and the turbulence-degraded measurements are  $P = 0.0618$  and  $P = 0.0464$ , respectively. The estimated classification result is based on the metal and dielectric DoLP priors adaptively updated by the higher-order super-Gaussian method discussed in Section 3.2.1. In the classification results, the blue color implies dielectric and the red color implies metal. The final estimates are obtained after 300 iterations.

the previous results. Similar to the higher-order super-Gaussian method, to classify the no-turbulence and the turbulence-degraded images, the threshold is computed by fitting the distribution of the DoLP measurements with the Gaussian function as described in Section 3.2.2. The resulting thresholds are  $P = 0.0932$  and  $P = 0.0747$  for the no-turbulence and turbulence-degraded data, respectively.

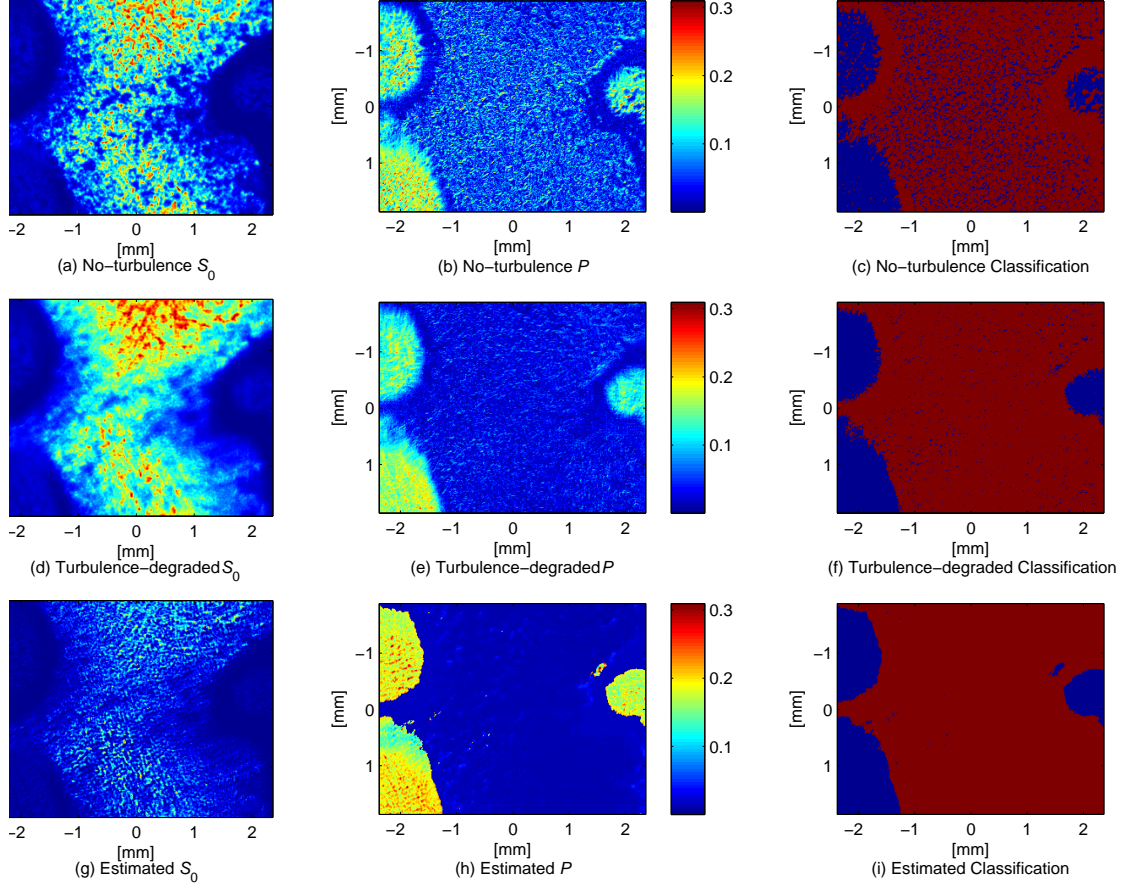


Figure 4.5: Results of the material-classification algorithm using adaptive DoLP priors derived from the Gaussian method for the painted aluminum target ( $\theta_i = \theta_r = 24^\circ$  and  $D/r_0 \approx 7.9$ ). The thresholds for classifying the no-turbulence and the turbulence-degraded measurements are  $P = 0.0932$  and  $P = 0.0747$ , respectively. The estimated classification result is based on the metal and dielectric DoLP priors adaptively updated by the Gaussian method discussed in Section 3.2.2. In the classification results, the blue color implies dielectric and the red color implies metal. The final estimates are obtained after 300 iterations.

Figure 4.5(i) shows that the algorithm using adaptive priors updated by the Gaussian method accurately classifies the target scene. Shown in Fig. 4.5(h) is the estimated  $P$  result. Note the clear contrast between the two material types which comprise the target scene. This result is a clear validation of this approach.

The estimated  $S_0$  result is similar to the result of the previous method. Although the  $S_0$  result seems to recover features lost in the turbulence-degraded images, it is difficult to objectively quantify this observation because of the aberrated no-turbulence

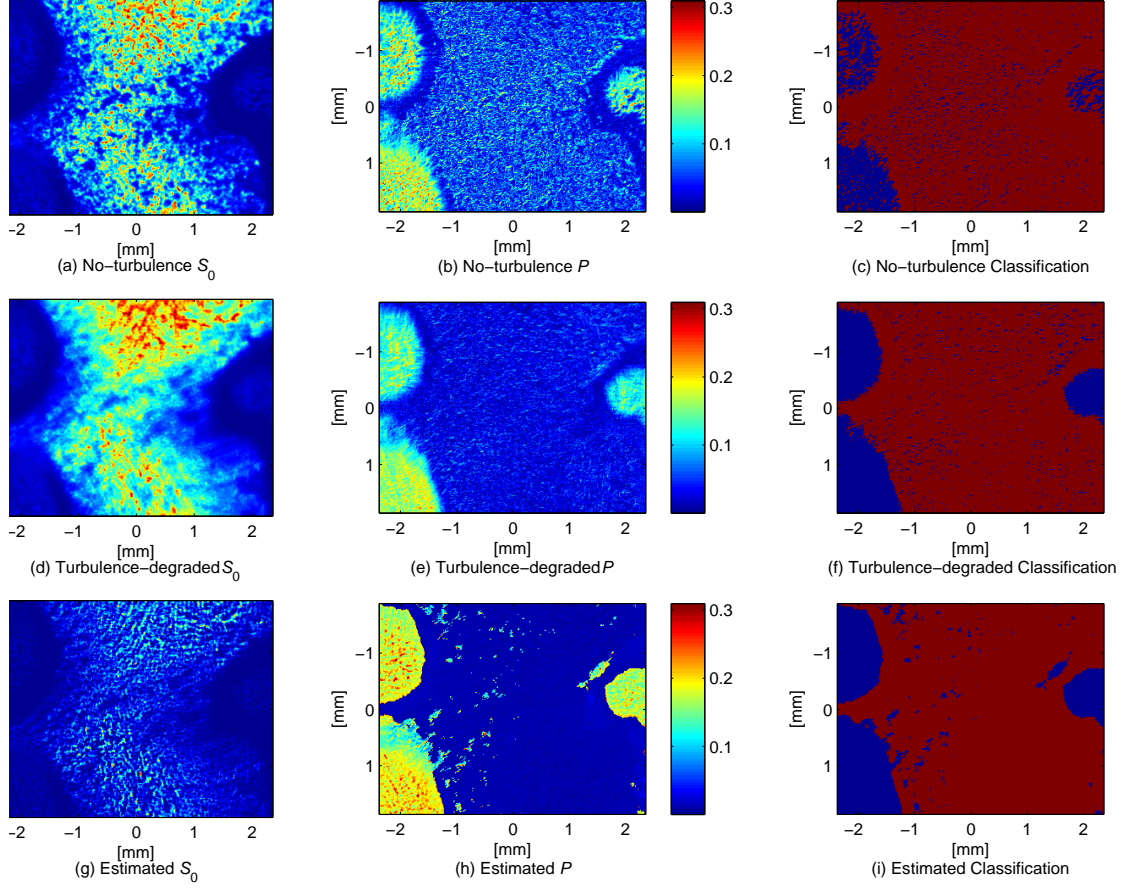


Figure 4.6: Results of the material-classification algorithm using adaptive DoLP priors derived from the distribution-averaging method for the painted aluminum target ( $\theta_i = \theta_r = 24^\circ$  and  $D/r_0 \approx 7.9$ ). The thresholds for classifying the no-turbulence and the turbulence-degraded measurements are  $P = 0.1223$  and  $P = 0.0651$ , respectively. The estimated classification result is based on the metal and dielectric DoLP priors adaptively updated by the distribution-averaging method discussed in Section 3.2.3. In the classification results, the blue color implies dielectric and the red color implies metal. The final estimates are obtained after 300 iterations.

images. As Section 3.3 briefly mentions, the no-turbulence images which are considered “truth” in this research for the basis of comparison do contain static imaging aberrations.

*4.3.3 Distribution-Averaging Method.* Figure 4.6 shows results of the material-classification algorithm using the distribution-averaging method developed in Section 3.2.3. The images of the target and the layout of the figure are identical to those

of the previous results. To classify the no-turbulence and the turbulence-degraded data, the threshold is computed by finding the mean of the distribution of the DoLP measurements. The corresponding thresholds are  $P = 0.1223$  and  $P = 0.0651$  for the no-turbulence and the turbulence-degraded data, respectively.

The estimated classification result in Fig. 4.6(i) shows that DoLP priors updated by the distribution-averaging method significantly improve the performance of the fixed-threshold based algorithm at the tested near-normal collection geometry. Performance is similar to the previously analyzed Gaussian method with some instances of misclassification occurring along the metal/dielectric boundaries. This may be an acceptable trade-off considering the computational simplicity of this technique.

Like the Gaussian method result, the estimated  $P$  result in Fig. 4.6(h) displays a clear contrast between the two material classes with features recovered after being lost in the turbulence-degraded images. The estimated  $S_0$  result does not display any noticeable differences from the  $S_0$  estimation results of the previous methods. Overall, the distribution-averaging method yields good results for such a computationally simplistic technique.

#### 4.4 *Spatial Analysis of the Classification Results*

Table 4.1 summarizes the material-classification results of the three proposed methods for the painted aluminum target at the near-normal collection geometry tested in this experiment. The table reports the results for three atmospheric turbulence conditions ( $D/r_0 \approx 7.9, 10.5$ , and  $12.9$ ). The first column indicates the method applied to update the DoLP priors. The second column indicates the image being analyzed, either turbulence-degraded (Turb.) or estimated (Est.) images. The last two columns contain the RMSE and the correlation coefficient of the classification results.

Table 4.1: Material-classification results for the painted aluminum target at  $\theta_i = \theta_r = 24^\circ$

Adaptive Method	Image	$D/r_0$	RMSE	Corr. Coeff.
Higher-Order Super-Gaussian Method	Turb.	7.9	0.575	0.336
	Est.	7.9	0.730	0.0337
	Turb.	10.5	0.581	0.306
	Est.	10.5	0.733	0.0080
	Turb.	12.9	0.595	0.286
	Est.	12.9	0.734	0.0095
Gaussian Method	Turb.	7.9	0.396	0.562
	Est.	7.9	0.391	0.573
	Turb.	10.5	0.399	0.555
	Est.	10.5	0.396	0.563
	Turb.	12.9	0.405	0.542
	Est.	12.9	0.409	0.534
Distribution- Averaging Method	Turb.	7.9	0.369	0.536
	Est.	7.9	0.376	0.529
	Turb.	10.5	0.383	0.514
	Est.	10.5	0.388	0.509
	Turb.	12.9	0.398	0.491
	Est.	12.9	0.393	0.498

The nearly-zero correlation coefficients of the higher-order super-Gaussian method in Table 4.1 conclusively show that this technique fails to accurately classify the target for the reason discussed previously.

The Gaussian method, whose computed threshold is the best approximation to empirical data among the three methods, shows slightly improved performance over the classification using turbulence-degraded images. These improvements, however, are quantitatively too minimal to validate the proposed algorithm. Thus, in order to evaluate the validity of the algorithm properly, it needs to be understood that the no-turbulence images (“truth”) contain static aberrations as previously mentioned. These aberrations penalize the estimated classification result when computing the RMSE and the correlation coefficient because the algorithm corrects these aberra-

tions as qualitatively shown in Figs. 4.5(h) and (i). Despite marginal quantitative improvements, the estimated  $P$  and classification results shown in Figs. 4.5(h) and (i) clearly depict that the Gaussian method classifies the target with greater accuracy than the turbulence-degraded images. Further analysis using no-turbulence images whose static aberrations are removed may provide more relevant image metrics for quantitative study of the classification results.

The metric results of the distribution-averaging method are similar to those of the Gaussian method in that improvements in performance increase as atmospheric turbulence becomes weaker ( $D/r_0$  decreases). Unlike the Gaussian update technique, however, the distribution-averaging method yields classification results which are quantitatively worse than the turbulence-degraded results. For the same reason discussed above, it can still be concluded that the distribution-averaging method improves the classification over the turbulence-degraded result based on Figs. 4.6(h) and (i). Note that Table 4.1 indicates that the Gaussian method provides results somewhat better than the distribution-averaging method. Considering the computational simplicity of the latter update technique, relatively small differences in performance may be an acceptable trade-off as suggested in Section 4.3.3.

## V. Conclusions and Future Work

### 5.1 Conclusions

In this thesis, a binary material-classification algorithm augmented with adaptive DoLP priors is developed for improved performance at near-normal collection geometries. The algorithm is based on Hyde’s material-classification technique which utilized fixed DoLP priors. Hyde’s algorithm used a variant of the multichannel blind-deconvolution technique developed by LeMaster and Cain to estimate  $S_0$ ,  $P$ , and  $h_c$  from polarimetric imagery degraded by atmospheric turbulence. To discriminate between metals and dielectrics, DoLP estimates from the blind-deconvolution results of each DoLP prior are used to compute the corresponding values of the objective function  $Q$ . Whichever DoLP prior maximizes  $Q$  determines the classification of the target at a given pixel location. A key limitation of this algorithm arises from the polarization behavior of light scattered from natural materials at near-normal collection geometries. The previously developed material-classification technique relied on fixed-threshold DoLP priors which performed poorly for near-normal collection geometries. To alleviate this limitation in collection geometries, this research developed methods to adaptively update the DoLP priors as more information about the scene became available.

Three methods are investigated for performing this update. The first method, called the higher-order super-Gaussian method, involves fitting the sum of two super-Gaussian functions to the measured distribution of DoLP estimates. This method is analytically sound, but suffers because the resulting fit poorly predicts the location of the threshold empirically evident in the estimated DoLP distributions. This results in misclassification of metal as dielectric at numerous pixels. The second method, called the Gaussian method, fits the distribution of DoLP estimates with the sum of two Gaussian functions. This approach is based on the observation that DoLP measurements (at a given surface state and collection geometry) are equivalent to a Poisson random variable divided by another Poisson random variable. This distribution has no analytical form but is Gaussian-like. It is clearly shown that the Gaussian method

computes the most accurate threshold. The last technique developed and analyzed in this thesis is the distribution-averaging method. This method is based on an empirical observation that the mean of the DoLP distribution approximately lies at the true threshold value. This simple approach produces classification results which are significantly improved over the existing fixed-prior method. Both RMSE and correlation coefficient calculations of experimental data confirm that the DoLP priors updated by the Gaussian method and the distribution-averaging method produce accurate classification results in the tested atmospheric turbulence conditions.

## 5.2 *Future Work*

*5.2.1 Testing Collection Geometry Region of Validity.* The first area of possible future work is to perform experiments on the proposed methods with collection geometries  $\theta_i, \theta_r < 24^\circ$ . Even though the adaptive approach developed in this research significantly extends the region of applicability of the algorithm beyond the existing method, the algorithm will eventually fail because the polarization difference between dielectrics and metals will become too small to be discerned. The collection geometry range of validity for the proposed methods has not been confirmed empirically. Experiments with collection geometries  $\theta_i, \theta_r < 24^\circ$  will allow one to fully understand the capabilities of the proposed techniques.

*5.2.2 Field Testing.* Next the proposed algorithm should be applied to a real-world scenario by conducting field experiments. A compact polarimeter would be needed for this purpose. Figure 5.1 depicts a polarization camera suitable for such field testing, which is also referred to in Hyde’s research. This camera is a commercial division of amplitude polarimeter with three polarization channels configured with  $0^\circ$ ,  $45^\circ$ , and  $90^\circ$  linear polarizers to measure the Stokes parameters  $S_0$ ,  $S_1$ , and  $S_2$ .

*5.2.3 Comparison of Material-Classification Results.* There exist other polarization-based material-classification techniques, such as Wolff’s polarization Fresnel ratio and Tominaga and Kimachi’s degree of polarization (DoP) map methods.



### Schematic View of 3-CCD Camera

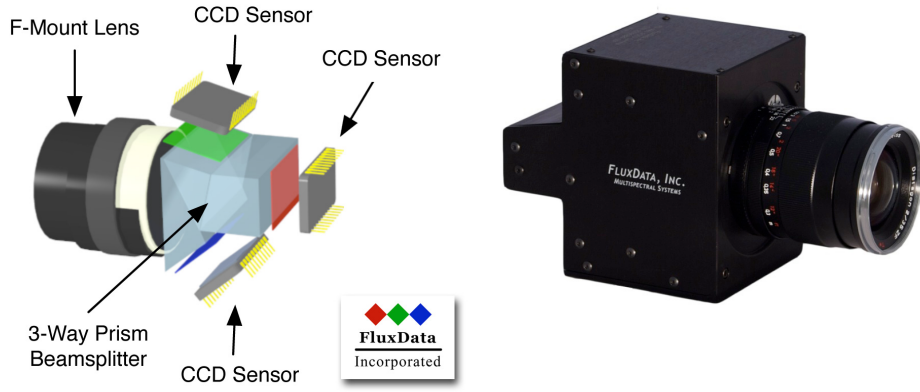


Figure 5.1: A three-channel polarization camera developed by FluxData, Inc. [5].

Wolff utilizes the Fresnel reflection coefficients to estimate the polarization Fresnel ratio whose value is used to discriminate between metals and dielectrics [27]. Tomimaga and Kimachi estimate the DoP from the irradiance through a polarizer and use the curvature of the DoP map to discriminate between the two material classes [24]. By comparing the results from these techniques, the relative accuracy/validity of the proposed methods can be assessed.

*5.2.4 Use of  $S_0$  Estimate to Aid Classification.* One thing not used in this research was the information contained in the  $S_0$  estimate. The rather obvious observation that metals tend to scatter light more strongly than dielectrics could be used to aid the polarization-based classification and extend the collection geometry range of validity of the algorithm even further.

*5.2.5 DoLP Derivative Classification.* While DoLP varies significantly versus incidence/observation angle and surface state, the rate of change of the DoLP remains fairly consistent over a wide range of conditions. Furthermore, the derivatives of the DoLPs of metals and dielectrics are very distinct with metals having a DoLP derivative of approximately zero and dielectrics having a large DoLP derivative (especially versus incidence/observation angle). This trend holds even for very near-normal collection geometries. For this approach to be implemented, the deconvolution

algorithm must be reworked to estimate the derivative of the DoLP or measurements at two slightly different observation angles need to be collected.

*5.2.6 Diffraction-Limited Truth Images.* The quantitative analysis of classification results shows that the no-turbulence (“truth”) images are of poor quality such that improvements in estimates brought about by the proposed algorithm are not evident in the objective measures. Using “diffraction-limited” no-turbulence images as truths may provide more relevant quantitative measures. This can be accomplished in two ways. The first, of course, is to collect new polarimetric images. This is now possible with the new polarimetric imager in the Optical Turbulence Estimation, Compensation, and Simulation laboratory. This instrument unfortunately was unavailable for this thesis. The second is to deconvolve the no-turbulence images. This was not done in this analysis to remain consistent with the algorithm comparison, performed by Hyde in [11].

## Bibliography

1. Andrews, L.C. and R.L. Phillips. *Laser beam propagation through random media*. SPIE Press Monograph. SPIE Press, 2005. ISBN 9780819459480.
2. Beil, A., R. Daum, R. Harig, and G. Matz. “Remote sensing of atmospheric pollution by passive FTIR spectrometry”. K. Schaefer (editor), *Society of Photo-Optical Instrumentation Engineers (SPIE) Conference Series*, volume 3493 of *Society of Photo-Optical Instrumentation Engineers (SPIE) Conference Series*, 32–43. December 1998.
3. Box, George E.P. and George C. Tiao. *Bayesian Inference in Statistical Analysis*. John Wiley & Sons, Inc., 1992. ISBN 9781118033197.
4. Coulson, K.L. *Polarization and intensity of light in the atmosphere*. Studies in geophysical optics and remote sensing. A. Deepak Pub., 1988. ISBN 9780937194126.
5. FluxData, Inc. “FD-1665 3-CCD Multispectral Camera”. URL <http://www.fluxdata.com/wp-content/uploads/FD-1665-brochure.pdf>.
6. Goldstein, D.H. and E. Collett. *Polarized light*. Optical engineering. Marcel Dekker, 2003. ISBN 9780824740535.
7. Goodman, J.W. *Statistical optics*. Wiley classics library. Wiley, 2000. ISBN 9780471399162.
8. Goodman, J.W. *Introduction to Fourier optics*. McGraw-Hill physical and quantum electronics series. Roberts & Co., 2005. ISBN 9780974707723.
9. Goudail, François, Patrick Terrier, Yoshitake Takakura, Laurent Bigué, Frédéric Galland, and Vincent DeVlaminck. “Target Detection with a Liquid-Crystal-Based Passive Stokes Polarimeter”. *Appl. Opt.*, 43(2):274–282, Jan 2004. URL <http://ao.osa.org/abstract.cfm?URI=ao-43-2-274>.
10. Hecht, E. *Optics*. Addison-Wesley, 2002. ISBN 9780805385663.
11. Hyde, M. W., IV. *Determining the index of refraction of an unknown object using passive polarimetric imagery degraded by atmospheric turbulence*. Ph.D. thesis, Air Force Institute of Technology, 2010.
12. Hyde, M.W., S.C. Cain, J.D. Schmidt, and M.J. Havrilla. “Material Classification of an Unknown Object Using Turbulence-Degraded Polarimetric Imagery”. *Geoscience and Remote Sensing, IEEE Transactions on*, 49(1):264–276, Jan. 2011. ISSN 0196-2892.
13. James, Stevens P. *Blind Deconvolution Through Polarization Diversity of Long Exposure Imagery*. Master’s thesis, Air Force Institute of Technology, 2009.
14. Kundur, D. and D. Hatzinakos. “Blind image deconvolution”. *Signal Processing Magazine, IEEE*, 13(3):43–64, may 1996. ISSN 1053-5888.

15. LeMaster, Daniel A. and Stephen C. Cain. “Multichannel blind deconvolution of polarimetric imagery”. *J. Opt. Soc. Am. A*, 25(9):2170–2176, Sep 2008. URL <http://josaa.osa.org/abstract.cfm?URI=josaa-25-9-2170>.
16. Matchko, Roy M. and Grant R. Gerhart. “Polarization azimuth angle in daylight scenes”. *Optical Engineering*, 44(2):028001, 2005. URL <http://link.aip.org/link/?JOE/44/028001/1>.
17. Moon, T.K. “The expectation-maximization algorithm”. *Signal Processing Magazine, IEEE*, 13(6):47–60, nov 1996. ISSN 1053-5888.
18. Roggemann, M.C. and B. Welsh. *Imaging through turbulence*. CRC Press laser and optical science and technology series. CRC Press, 1996. ISBN 9780849337871.
19. Schmidt, J.D. *Numerical simulation of optical wave propagation with examples in MATLAB*. Press Monograph. SPIE, 2010. ISBN 9780819483263.
20. Schott, J.R. *Fundamentals of polarimetric remote sensing*. Tutorial texts series. SPIE Press, 2009. ISBN 9780819475343.
21. Schulz, Timothy J. “Multiframe blind deconvolution of astronomical images”. *J. Opt. Soc. Am. A*, 10(5):1064–1073, May 1993. URL <http://josaa.osa.org/abstract.cfm?URI=josaa-10-5-1064>.
22. Thilak, V., C.D. Creusere, and D.G. Voelz. “Passive Polarimetric Imagery Based Material Classification For Remote Sensing Applications”. *Image Analysis and Interpretation, 2008. SSIAI 2008. IEEE Southwest Symposium on*, 153–156. march 2008.
23. Thilak, Vimal, David G. Voelz, and Charles D. Creusere. “Polarization-based index of refraction and reflection angle estimation for remote sensing applications”. *Appl. Opt.*, 46(30):7527–7536, Oct 2007. URL <http://ao.osa.org/abstract.cfm?URI=ao-46-30-7527>.
24. Tominaga, Shoji and Akira Kimachi. “Polarization imaging for material classification”. *Optical Engineering*, 47(12):123201, 2008. URL <http://link.aip.org/link/?JOE/47/123201/1>.
25. Trees, H.L.V. *Detection, estimation, and modulation theory*. Number pt. 1 in Detection, Estimation, and Modulation Theory. Wiley-Interscience. ISBN 9780471095170.
26. Tyo, J. Scott, Dennis L. Goldstein, David B. Chenault, and Joseph A. Shaw. “Review of passive imaging polarimetry for remote sensing applications”. *Appl. Opt.*, 45(22):5453–5469, Aug 2006. URL <http://ao.osa.org/abstract.cfm?URI=ao-45-22-5453>.
27. Wolff, L. B. “Polarization-Based Material Classification from Specular Reflection”. *IEEE Trans. Pattern Anal. Mach. Intell.*, 12:1059–1071, November 1990. ISSN 0162-8828.

28. Zallat, J., P. Grabbling, and Y. Takakura. “Using polarimetric imaging for material classification”. *Image Processing, 2003. ICIP 2003. Proceedings. 2003 International Conference on*, volume 2, II – 827–30 vol.3. sept. 2003. ISSN 1522-4880.

REPORT DOCUMENTATION PAGE					Form Approved OMB No. 0704-0188	
<p>The public reporting burden for this collection of information is estimated to average 1 hour per response, including the time for reviewing instructions, searching existing data sources, gathering and maintaining the data needed, and completing and reviewing the collection of information. Send comments regarding this burden estimate or any other aspect of this collection of information, including suggestions for reducing this burden to Department of Defense, Washington Headquarters Services, Directorate for Information Operations and Reports (0704-0188), 1215 Jefferson Davis Highway, Suite 1204, Arlington, VA 22202-4302. Respondents should be aware that notwithstanding any other provision of law, no person shall be subject to any penalty for failing to comply with a collection of information if it does not display a currently valid OMB control number. <b>PLEASE DO NOT RETURN YOUR FORM TO THE ABOVE ADDRESS.</b></p>						
1. REPORT DATE (DD-MM-YYYY)		2. REPORT TYPE		3. DATES COVERED (From — To)		
22-03-2012		Master's Thesis		Sept 2010 — Mar 2012		
4. TITLE AND SUBTITLE  Binary Classification of an Unknown Object through Atmospheric Turbulence Using a Polarimetric Blind-Deconvolution Algorithm Augmented with Adaptive Degree of Linear Polarization Priors				5a. CONTRACT NUMBER		
				5b. GRANT NUMBER F2KBAH0323G001		
				5c. PROGRAM ELEMENT NUMBER		
				5d. PROJECT NUMBER ENGJON169		
6. AUTHOR(S)  Kim, Mu J., Capt, USAF				5e. TASK NUMBER		
				5f. WORK UNIT NUMBER		
7. PERFORMING ORGANIZATION NAME(S) AND ADDRESS(ES) Air Force Institute of Technology Graduate School of Engineering and Management (AFIT/EN) 2950 Hobson Way WPAFB OH 45433-7765				8. PERFORMING ORGANIZATION REPORT NUMBER  AFIT/GE/ENG/12-26		
9. SPONSORING / MONITORING AGENCY NAME(S) AND ADDRESS(ES) Air Force Maui Optical and Supercomputing Site Capt Casey J. Pellizzari 535 Lipoa Pkwy, Suite 200 Kihei, HI 96753 (808) 874-1538, Casey.Pellizzari@maui.afmc.af.mil				10. SPONSOR/MONITOR'S ACRONYM(S) AFRL/RDSM		
				11. SPONSOR/MONITOR'S REPORT NUMBER(S)		
12. DISTRIBUTION / AVAILABILITY STATEMENT  APPROVED FOR PUBLIC RELEASE; DISTRIBUTION UNLIMITED.						
13. SUPPLEMENTARY NOTES  This material is declared a work of the U.S. Government and is not subject to copyright protection in the United States.						
14. ABSTRACT This research develops an enhanced material-classification algorithm to discriminate between metals and dielectrics using passive polarimetric imagery degraded by atmospheric turbulence. To improve the performance of the existing technique for near-normal collection geometries, the proposed algorithm adaptively updates the degree of linear polarization (DoLP) priors as more information becomes available about the scene. Three adaptive approaches are presented. The higher-order super-Gaussian method fits the distribution of DoLP estimates with a sum of two super-Gaussian functions to update the priors. The Gaussian method computes the classification threshold value, from which the priors are updated, by fitting the distribution of DoLP estimates with a sum of two Gaussian functions. Lastly, the distribution-averaging method approximates the threshold value by finding the mean of the DoLP distribution. The experimental results confirm that the new adaptive method significantly extends the collection geometry range of validity for the existing technique.						
15. SUBJECT TERMS  Polarimetric Imagery, Blind Deconvolution, Material Classification, Passive Remote Sensing						
16. SECURITY CLASSIFICATION OF:			17. LIMITATION OF ABSTRACT	18. NUMBER OF PAGES	19a. NAME OF RESPONSIBLE PERSON	
a. REPORT	b. ABSTRACT	c. THIS PAGE			Milo W. Hyde IV, Major, USAF (ENG)	
U	U	U	UU	70	19b. TELEPHONE NUMBER (include area code) (937) 255-3636, x4371; milo.hyde@afit.edu	